Domino-style earthquakes along blind normal faults in Northern Thessaly (Greece): kinematic evidence from field observations, seismology, SAR interferometry and GNSS

Athanassios Ganas, Sotiris Valkaniotis, Pierre Briole, Anna Serpetsidaki, Vassilis Kapetanidis, Ilektra Karasante, Ioannis Kassaras, George Papathanassiou, Ioannis Karamitros, Varvara Tsironi, et al.

Bulletin of the Geological Society of Greece

Vol 58 (2021)

Special Issue on the 2021 Northern Thessaly, Greece, Earthquake Sequence

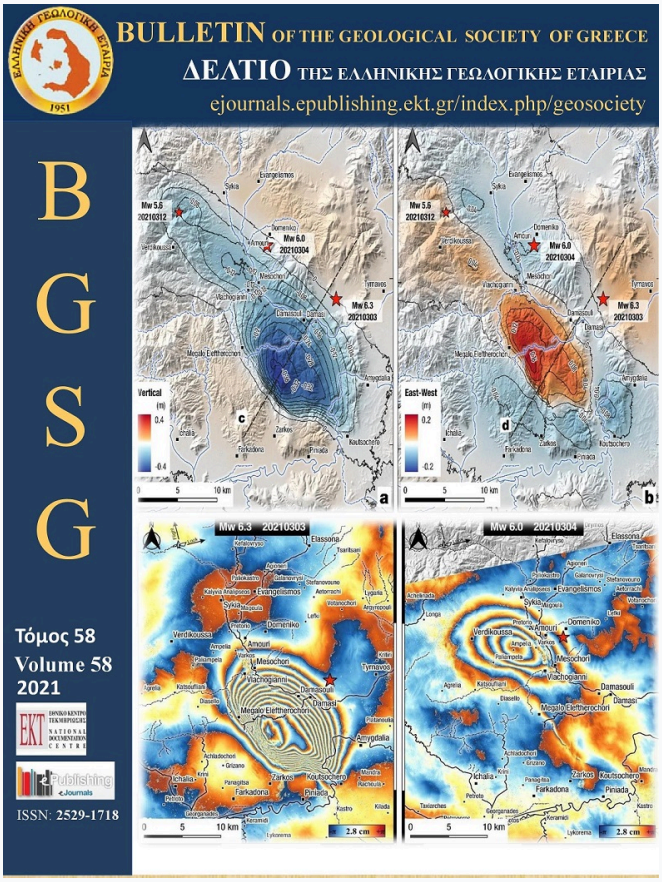

Domino-style earthquakes along blind normal faults in Northern Thessaly (Greece): kinematic evidence from field observations, seismology, SAR interferometry and GNSS

Athanassios Ganas, Sotiris Valkaniotis, Pierre Briole, Anna Serpetsidaki, Vassilis Kapetanidis, Ilektra Karasante, Ioannis Kassaras, George Papathanassiou, Ioannis Karamitros, Varvara Tsironi, Panagiotis Elias, Vasilis Sarhosis, Andreas Karakonstantis, Emmanouela Konstantakopoulou, Panagiotis Papadimitriou, Efthimios Sokos

doi: 10.12681/bgsg.27102

BGSG

Volume 58

Research Paper

DOMINO-STYLE EARTHQUAKES ALONG BLIND NORMAL FAULTS IN NORTHERN THESSALY (GREECE): KINEMATIC EVIDENCE FROM FIELD OBSERVATIONS, SEISMOLOGY, SAR INTERFEROMETRY AND GNSS

Athanassios Ganas[1], Sotiris Valkaniotis[2], Pierre Briole[3], Anna Serpetsidaki[4], Vasilis Kapetanidis[5], Ilektra Karasante[1], Ioannis Kassaras[5], George Papathanassiou[2], Ioannis Karamitros[1], Varvara Tsironi[1,4], Panagiotis Elias[6], Vasilis Sarhosis[7], Andreas Karakonstantis[5], Emmanouela Konstantakopoulou[1,5], Panagiotis Papadimitriou[5], and Efthimios Sokos[4]

[1]National Observatory of Athens, Institute of Geodynamics, Lofos Nymfon, Thission, 11810 Athens, Greece

aganas@noa.gr, vtsironi@noa.gr, hlekara@hotmail.com, jkaram@noa.gr, emma.kon97@gmail.com,

[2]Department of Civil Engineering, Democritus University of Thrace, 67100 Xanthi, Greece

valkaniotis@yahoo.com, gpapatha@civil.duth.gr,

[3]Ecole Normale Supérieure de Paris, PSL Research University, Laboratoire de Géologie - UMR CNRS 8538, 24 rue Lhomond, 75005 Paris – France

briole@ens.fr,

[4]Seismological Laboratory, Department of Geology, University of Patras, 26504 Rio, Greece

annaserp@upatras.gr, esokos@upatras.gr,

[5]Seismological Laboratory, Department of Geology and Geoenvironment, National and Kapodistrian University of Athens, Greece

ppapadim@geol.uoa.gr, vkapetan@geol.uoa.gr, kassaras@geol.uoa.gr, akarakon@geol.uoa.gr,

[6]National Observatory of Athens, Institute of Astronomy, Astrophysics, Space Applications and Remote Sensing, Vas. Pavlou and I. Metaxa, GR-15 236 Penteli, Greece;

pelias@noa.gr,

[7]School of Civil Engineering, University of Leeds, UK

v.sarhosis@leeds.ac.uk,

*Correspondence: aganas@noa.gr, Tel.: +30 210 3490186 (A.G.)

Correspondence to:
Athanasios Ganas
aganas@noa.gr

DOI number:
http://dx.doi.org/10.12681/bgsg.27102

Keywords:
Thessaly; earthquake; InSAR; relocation; GNSS; stress transfer; blind fault; extension

Citation:
Ganas, A., Valkaniotis, S., Briole, P., Serpetsidaki, A., Kapetanidis, V., Karasante, I., Kassaras, I., Papathanassiou, G., Karamitros, I., Tsironi, V., Elias, P., Sarhosis, V., Karakonstantis, A., Konstantakopoulou, E., Papadimitriou, P. and Sokos, E. (2019), Domino-Style Earthquakes Along Blind Normal Faults in Northern Thessaly (Greece): Kinematic Evidence from Field Observations, Seismology, Sar Interferometry and GNSS. Bulletin Geological Society of Greece, 58, 37-86.

Publication History:
Received: 20/05/2021
Accepted: 07/07/2021
Accepted article online: 09/07/2021

The Editor wishes to thank Prof. V. Karakostas and Prof. R. Caputo for their work with the scientific reviewing of the manuscript and Ms Emmanouela Konstantakopoulou for editorial assistance.

Abstract

Here we present a joint analysis of the geodetic, seismological and geological data of the March 2021 Northern Thessaly seismic sequence, that were gathered and processed as of April 30, 2021. First, we relocated seismicity data from regional and local networks and inferred the dip-direction (NE) and dip-angle (38°) of the March 3, 2021 rupture plane. Furthermore, we used ascending and descending SAR images acquired by the Sentinel-1 satellites to map the co-seismic displacement field. Our results indicate that the March 3, 2021 Mw=6.3 rupture occurred on a NE-dipping, 39° normal fault located between the villages Zarko (Trikala) and Damasi (Larissa). The event of March 4, 2021 occurred northwest of Damasi, along a fault oriented WNW-ESE and produced less deformation than the event of the previous day. The third event occurred on March 12, 2021 along a south-dipping normal fault. We computed 22 focal mechanisms of aftershocks with M≥4.0 using P-wave first motion polarities. Nearly all focal mechanisms exhibit normal kinematics or have a dominant normal dip-slip component. The use of InSAR was crucial to differentiate the ground deformation between the ruptures. The majority of deformation occurs in the vertical component, with a maximum of 0.39 m of subsidence over the Mw=6.3 rupture plane, south and west of Damasi. A total amount of 0.3 m horizontal displacement (E-W) was measured. We also used GNSS data (at 30-s sampling interval) from twelve permanent stations near the epicentres to obtain 3D seismic offsets of station positions. Only the first event produces significant displacement at the GNSS stations (as predicted by the fault models, themselves very well constrained by InSAR). We calculated several post-seismic interferograms, yet we have observed that there is almost no post-seismic deformation, except in the footwall area (Zarkos mountain). This post-seismic deformation is below the 7 mm level (quarter of a fringe) in the near field and below the 1 mm level at the GNSS sites. The cascading activation of the three events in a SE to NW direction points to a pattern of domino-style earthquakes, along neighbouring fault segments. The kinematics of the ruptures point to a counter-clockwise change in the extension direction of the upper crust (from NE-SW near Damasi to N-S towards northwest, near Verdikoussa).

Keywords: Thessaly; earthquake; InSAR; relocation; GNSS; stress transfer; blind fault; extension

Περίληψη

Μέσω της εργασίας αυτής, παρουσιάζουμε μια πολύπλευρη ανάλυση γεωδαιτικών, σεισμολογικών και γεωλογικών δεδομένων της σεισμικής ακολουθίας του Μαρτίου 2021 στη Βόρεια Θεσσαλία. Για την ανάλυση αυτή, χρησιμοποιήθηκαν δεδομένα έως και τις 30 Απριλίου 2021. Πρώτα, έγινε ο επαναπροσδιορισμός των σεισμικών επικέντρων των σεισμολογικών δεδομένων με την παροχή δεδομένων από τοπικά σεισμολογικά δίκτυα και βρέθηκε η φορά κλίσης (ΒΑ) και η γωνία κλίσης (38°) του σεισμικού ρήγματος του σεισμού της 3ης Μαρτίου 2021. Στη συνέχεια, χρησιμοποιήθηκαν δεδομένα εικόνων ραντάρ ανοδικής και καθοδικής τροχιάς από τους δορυφόρους Sentinel-1 της ESA για την χαρτογράφηση της συν-σεισμικής παραμόρφωσης που προκλήθηκε από τους σεισμούς. Τα αποτελέσματα μας υποδεικνύουν ότι η κύρια διάρρηξη του σεισμικού γεγονότος στις 3 Μαρτίου μεγέθους Mw=6.3 ενεργοποίησε ένα κανονικού τύπου «τυφλό» ρήγμα, που κλίνει προς τα ΒΑ με 39 μοίρες κλίση και βρίσκεται μεταξύ των χωριών Ζάρκο (Τρίκαλα) και Δαμάσι (Λάρισα). Το σεισμικό γεγονός της 4ης Μαρτίου 2021, που έγινε βορειοδυτικά του Δαμασίου, διέρρηξε ένα ρήγμα με μέση διεύθυνση ΔΒΔ-ΑΝΑ και παρήγαγε λιγότερη εδαφική παραμόρφωση σε σχέση με το πρώτο. Το τρίτο σεισμικό γεγονός έλαβε χώρα στις 12 Μαρτίου 2021, κατά μήκος ενός κανονικού ρήγματος που κλίνει προς το νότο. Στη συνέχεια, ο υπολογισμός 22 μηχανισμών γένεσης από μετασεισμούς μεγέθους M>4.0 έγινε με βάση την μέθοδο των πρώτων αποκλίσεων των P σεισμικών κυμάτων. Σχεδόν όλοι οι μηχανισμοί γένεσης δείχνουν κινηματική κανονικών ρηγμάτων ή ότι η κανονική κινηματική των ρηγμάτων είναι η επικρατούσα. Η χρήση της Συμβολομετρίας Ραντάρ είναι καθοριστική στην ερμηνεία των σεισμών αυτών καθότι με αυτή μπορέσαμε να προσδιορίσουμε χωρικά την διαφοροποίηση της παραμόρφωσης του εδάφους μεταξύ των σεισμικών διαρρήξεων από τον εκάστοτε σεισμό. Το μεγαλύτερο ποσοστό της παραμόρφωσης παρατηρήθηκε στη κατακόρυφη συνιστώσα της κίνησης, με μέγιστη καθίζηση 0.39 m στην περιοχή πάνω από το ρήγμα του πρώτου σεισμού Mw=6.3, νότια του χωριού Δαμάσι. Επίσης, μετρήθηκε μία συνολική κίνηση της τάξεως των 0.3 m στην οριζόντια συνιστώσα Α-Δ. Επιπρόσθετα, χρησιμοποιήθηκαν δεδομένα GNSS (με ρυθμό δειγματοληψίας σήματος τα 30 s) από 12 μόνιμους σταθμούς της Θεσσαλίας έτσι ώστε να μετρηθεί το τρισδιάστατο άνυσμα της σεισμικής κίνησης του εκάστοτε σταθμού. Μόνο ο πρώτος σεισμός παρήγαγε σημαντικές μετατοπίσεις της θέσης των γεωδαιτικών σταθμών GNSS (όπως το είχαν προβλέψει και τα μοντέλα σεισμικών ρηγμάτων, που παρήχθησαν από τα δεδομένα της συμβολομετρίας ραντάρ). Επίσης, δεν παρατηρήθηκε κάποια μετασεισμική παραμόρφωση στα συμβολογράμματα ραντάρ, εκτός από την περιοχή που είναι το ανερχόμενο τέμαχος του ρήγματος του πρώτου σεισμού, στο βουνό Ζάρκο. Αυτή η μετασεισμική παραμόρφωση βρίσκεται κάτω από το όριο των 7 mm και κάτω από 1 mm σε περιοχές κοντά σε GNSS σταθμούς. Η διαδοχική ενεργοποίηση των τριών

σεισμών με διεύθυνση από τα ΝΑ προς τα ΒΔ δείχνει ένα χαρακτηριστικό τύπο ντόμινο διάρρηξης, κατά μήκος γειτονικών ρηγμάτων. Η κινηματική των διαρρήξεων που παρήγαγαν αυτούς τους σεισμούς δείχνουν μια αριστερόστροφη αλλαγή στην διεύθυνση του εφελκυσμού του άνω φλοιού (από ΒΑ-ΝΔ κοντά στο χωριό Δαμάσι σε Β-Ν προς βορειοδυτικά, κοντά στο χωριό Βερδικούσσα).

Λέξεις – Κλειδιά: Θεσσαλία, σεισμός, InSAR, επαναπροσδιορισμός σεισμών, GNSS, μεταφορά τάσης, «τυφλό» ρήγμα, εφελκυσμός.

1. INTRODUCTION

The region of Thessaly, in Central Greece is part of the Pelagonian zone which forms the western Internal Hellenides. It is characterised by abundant occurrences of crystalline basement, predominantly pre-Alpine in age. The Pelagonian is defined as a NW-SE trending zone consisting of thrust sheets that record Alpine orogenic events and is bordered by the Neotethys/Vardar oceanic suture zone in the NE and the external Hellenides (Pindos and Adria) in the SW (Mountrakis, 1984; Kilias and Mountrakis, 1989). The basement of the Thessaly region comprises a complexly deformed assemblage of quartzo-feldspathic gneiss and schist, mid-Mesozoic ultramafic ophiolite fragments, late Palaeozoic to Mesozoic marble and early Paleogene flysch, as well as mafic and calcareous schists.

Thessaly is located at the western end of the North Anatolian Fault Zone (NAFZ; a large transcurrent structure in the East Mediterranean), where the right-lateral strike slip ends and crustal extension prevails in mainland Greece (Fig. 1; Kiratzi et al. 1991; Taymaz et al. 1991; Hatzfeld et al. 1999; Papadimitriou and Karakostas, 2003; Müller et al., 2013; Konstantinou, 2017; Briole et al. 2021). The most prominent structural and geomorphic features strike NW-SE, such as the coastal and interior mountain ranges, their bounding faults and the late Tertiary sedimentary basins (Caputo and Pavlides, 1993). However, the Middle-Late Quaternary-to-present tectonic regime has formed WNW-ESE and E-W high angle, normal and oblique-slip faults (Mountrakis et al., 1993; Caputo and Pavlides, 1993; Caputo, 1995; 1996; Pavlides et al. 2004; Palyvos et al., 2010; Mantovani et al. 2018). The recent activity of these structures is confirmed by the location of both moderate and large magnitude earthquakes during the 20th century (Papazachos et al., 1983, 1993; Papastamatiou and Mouyaris, 1986; Pavlides, 1993; Hatzfeld et al., 1999), and by paleoseismological data (e.g., Caputo et al., 2004; Caputo and Helly, 2005; Palyvos et al., 2010; Tsodoulos et al. 2016). In northern

Thessaly, the strike of the active structures acquires a WNW-ESE orientation (Caputo and Pavlides, 1993; Ganas, 2020). This orientation of crustal stretching is probably a kinematic response to a change in the orientation of the regional stress field with respect to the NW-SE extension across the neighbouring rift systems of western and central Macedonia (Konstantinou et al. 2016). For example, the 1995 earthquake of Grevena - Kozani ruptured an ENE-WSW striking normal fault (Rigo et al. 2004). New strain rate data for west-central Macedonia and Thessaly (D'Agostino et al. 2020) also show a rotation of the dilatational strain axis from NW-SE to N-S across north Thessaly.

The epicentral area of the March 2021 earthquakes is characterised by low seismicity and low strain rates (~30 ns/yr; D'Agostino et al. 2020) while this area is located within the, Pindos crustal block as defined by kinematic criteria by Briole et al. (2021). The crustal thickness is about 35 km with the Moho dipping towards the west beneath the Pindos range (Grigoriadis et al. 2016). The March 3, 2021 10:16 UTC (Mw=6.3) shallow earthquake occurred near Damasi, about 20 km to the northwest of Larissa (Fig. 1; Lekkas et al. 2021; Ganas et al. 2021a; Valkaniotis et al. 2021; Tolomei et al. 2021). Then, a Mw=6.0 shallow earthquake occurred on March 4, 2021 18:38 UTC beneath the sedimentary basin of the Titarissios river. On March 12, 2021 12:57 UTC a third event of Mw=5.6 occurred near the NW edge of the Titarissios basin. The PGA due to the first event was measured as ~0.14 g at one strong-motion instrument in Larissa (Karakostas, 2021; Fig. 1).

In Table 1 we summarize the focal parameters of the three largest shocks of the sequence, as they have been determined by international agencies from moment tensor (MT) inversions. We observe that the events are located in the upper crust, with median depth ranging between 10 and 11 km. Some discrepancies occur, i.e., the shallow centroid depth obtained for the event on March 3, 2021 by NOA (4 km) compared to the solution by UOA (19 km); and for the centroid depth of March 4, 2021 by UOA (15 km) and GFZ (17 km), likely the result of unmodelled velocity structure. Both Mw and nodal planes of the GFZ solution for the event of 4 March 2021 diverge from the solutions provided by UOA, NOA and AUTH, likely the result of the poor data quality, the latter being likely the reason that MT is available from only four institutes for this event, despite its large size. In particular, the teleseismic inversions for the March 4, 2021 18:38 UTC event might be affected by the Kermadec Island event of Mw=7.4 (USGS), on 17:41 UTC since teleseismic inversions based mainly on surface waves are more vulnerable to this wave interference compared to local/regional body-wave inversions. The median values of the dip-angles of the MTs indicate shallow, intermediate-dipping normal faulting (≤40°), in agreement with the preliminary results

from the inversion of geodesy data and field observations that indicated the activation of three previously unknown normal faults (Ganas et al., 2021a). In addition, when considering the dip direction of the median nodal planes in Table 1, a counterclockwise rotation of ~30° is observed between the strike of the event on March 3, 2021 and the events on the 4th and 12th of March.

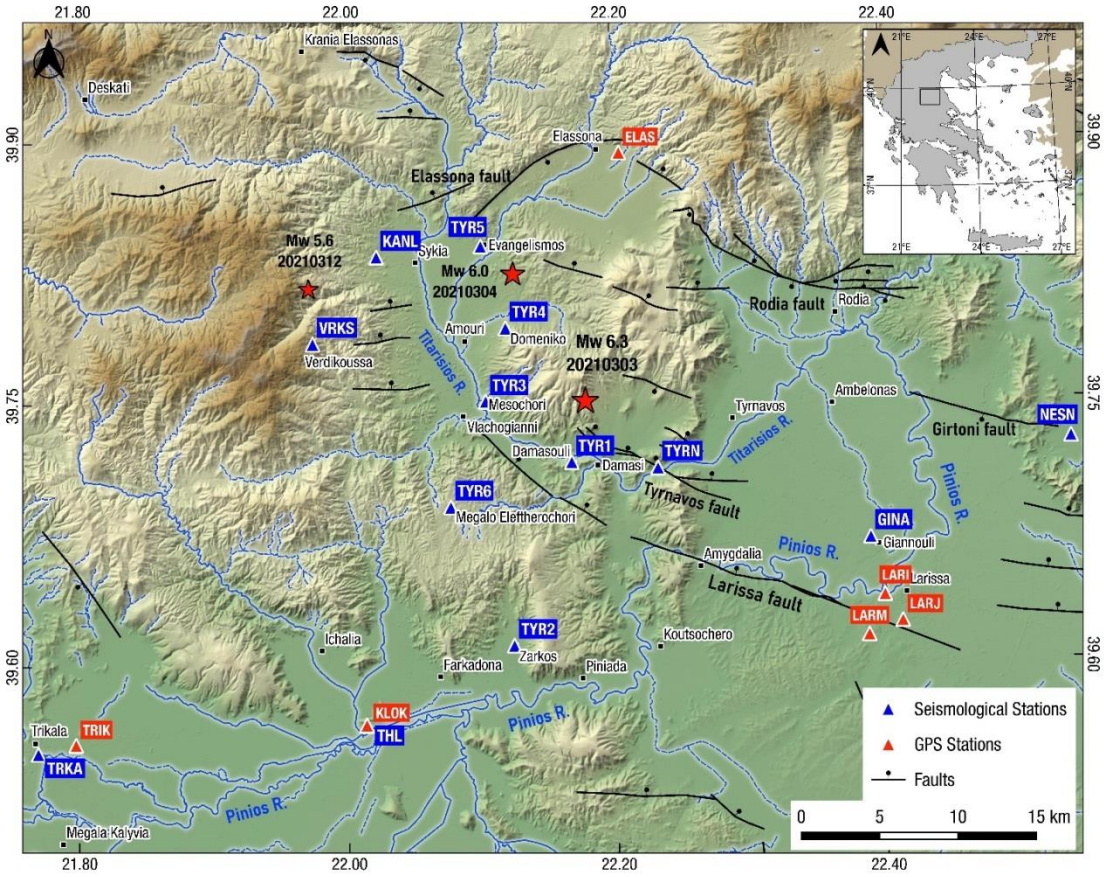

Fig. 1: Shaded relief map of the northern Thessaly 2021 earthquake area. Solid stars indicate relocated mainshock epicentres (this study). Blue triangles indicate the locations of the seismological stations. Red triangles represent permanent GNSS stations. Inset box at upper right shows study area within Greece. Black lines are active faults from the NOAFAULTs database http://doi.org/10.5281/zenodo.3483136 (with ticks at the downthrown side; modified from Caputo, 1990; 1995) and faults determined by our field work (this study). *A high-resolution version of this figure is provided in the supplement section of this article*.

In this study we present an analysis of seismological, geological and geodetic data that constrain the location and geometry of the activated faults. We relocated hundreds of aftershocks and computed the focal mechanisms for events with M≥4.0. Due to the shallow depth of the earthquakes (ranging from 5 to 15 km) and the good coherence of the area, it was possible to accurately map the surface deformation using InSAR. The interferograms show three main lobes of subsidence, partially overlapping, with a NW-SE orientation. We then processed GNSS data from twelve permanent stations located

at distances ranging from 15 to 40 km. The displacement data were inverted to model the dislocation sources assuming a homogeneous elastic half space. The inversion modelling confirms the activation of three normal faults, previously unknown. The earthquakes generated numerous secondary phenomena with vast areas of alluvial deposits exhibiting spectacular liquefaction features. No tectonic surface ruptures were found in the field, in agreement with the modelled faults. However, several NW-SE surface breaks were observed north of village Zarko (Fig. 1), aligned with the vanishing gradient of the interferometric phase of the first event (March 3, 2021). We interpret those as tensional cracks related to the dilatational strain of the rupture. Our study highlights the rotation of the stress field in this key region of central Greece and the particular type of strain release, that is by clustering of earthquakes along blind normal faults that ruptured in an unprecedented domino pattern involving three mainshocks.

2. ANALYSIS OF SEISMOLOGICAL DATA

2.1. Relocation of Seismicity

The mainshocks and aftershocks of the sequence were recorded by the broad-band and strong motion stations of the Hellenic Unified Seismological Network (HUSN; http://eida.gein.noa.gr/); moreover, seven (7) temporary stations were installed on March 5, 2021 in the epicentral area by AUTH (Department of Geophysics of the Aristotle University of Thessaloniki; HT network; doi:10.7914/SN/HT). These stations were named as TYR1-6 (Fig. 1) and they were equipped with Nanometrics hardware i.e., Trillium Compact (TC120) seismometers and Centaur recorders. Two (2) more temporary stations were installed on March 14, 2021 by the University of Patras Seismology Lab (UPSL; HP network; doi:10.7914/SN/HP), with GEOBIT-instruments equipment, i.e., the Geotiny Seismometer (KANL; Analipsi site; Fig. 1) and the GEOsix datalogger combined with GEOfba200 accelerometer and TC120 Seismometer (VRKS; Verdikoussa site; Fig. 1). The manually picked events by Institute of Geodynamics of the National Observatory of Athens NOA, during the first 30 days, were used for the initial location. Several velocity models were examined during the location procedure such as Hatzfeld et al., (1997), Drakatos et al., (1998), Novotny et al., (2001), Karastathis et al., (2011); the comparison was initially performed on the HYPOINVERSE location errors and the hypocentres' distribution. The crustal model suggested by Hatzfeld et al., (1997) was finally selected since it yielded the lowest errors (i.e., mean RMS ~ 0.13 s) with a Vp/Vs ratio value of 1.76, as also suggested by Hatzfeld et al. (1997).

Table 1 (next page). Source parameters of the three mainshocks from various agencies (https://www.seismicportal.eu/mtws/). (*) GFZ solution excluded (see text for discussion).

Origin time (UTC) YYYYMMDD	Lat. (°)	Lon. (°)	Source	Mw	Z (km)	Strike (°)	Dip (°)	Rake (°)
2021-03-03 10:16:08.3	39.76	22.21	USGS	6.3	12	307	36	-100
			GCMT	6.3	12	324	48	-72
			CPPT	6.3	12	321	36	-77
			GFZ	6.3	10	310	44	-89
			UOA	6.3	19	309	36	-91
			ERD	6.2	7	332	43	-85
			IPGP	6.2	10	321	33	-78
			KOERI	6.3	10	323	53	-79
			OCA	6.2	7	315	45	-90
			INGV	6.3	10	327	53	-70
			NOA	6.3	4	305	33	-108
			AUTH	6.2	6	314	36	-88
			Median	**6.3**	**10**	**318**	**39**	**-87**
			Stdev	**0.05**	**4**	**9**	**7**	**11**
2021-03-04 18:38:17.1	39.78	22.12	UOA	6.1	15	308	50	-92
			GFZ	6.3	17	329	41	-88
			NOA	6	8	287	31	-95
			AUTH	5.9	7	287	30	-92
			Median	**6.1**	**11**	**298**	**36**	**-92**
			Stdev	**0.2**	**5**	**20**	**9**	**3**
			Median*	**6.0**	**8**	**287**	**31**	**-92**
			Stdev*	**0.1**	**4**	**12**	**11**	**2**
2021-03-12 12:57:50.7	39.84	22.01	CPPT	5.5	18	109	41	-92
			INGV	5.6	10	96	37	-133
			GFZ	5.5	10	120	40	-85
			KOERI	5.5	10	108	38	-108
			GCMT	5.6	12	87	42	-109
			Median	**5.5**	**10**	**108**	**40**	**-108**
			Stdev	**0.1**	**4**	**13**	**2**	**19**

Subsequently, the double difference relocation HYPODD (Waldhauser, 2001) procedure was performed for two time periods, i.e., before and after the installation of the local stations. The relocation combined the P- and S- wave arrival times from 66007 phase picks in total, derived from fourteen (14) stations within 90 km from the mainshocks epicentral area for the first period and ten (10) stations within 30 km for the operation period of the local stations (Fig. 1) including data from three strong motion stations in the near field (TRKA, GINA and SOFA). HYPODD determines relative locations within clusters, using the double difference algorithm, developed by

Waldhauser and Ellsworth (2000). It improves relative location accuracy by strongly reducing the influence of the velocity structure on locations. The double-difference residuals for the pairs of earthquakes at each station were minimized by weighted least-squares, using the method of conjugate gradient (LSQR). The velocity model used in the relocation was the same with the model used in the initial location process. In total, 855 events were relocated and clustered in the area of interest with magnitude M_L between 0.8 and 6.0 (see Fig. S1; see Table S1 for a list of the relocated epicentres of the three main events). The HYPODD final results include the 89.2% of the initial dataset. The relocated hypocentres have an estimated mean rms residual of 4 ms and the mean location formal uncertainties x, y, z and t were 24 m, 25 m, 27 m and 11 ms, respectively for both periods. The relocated events are densely distributed, in three major clusters (Fig. 2 shown in boxes), activated in diverse times. The main activity is concentrated at the central area during the first 2-day period, March 3-4, 2021 (Fig. 3; cross section B_1B_2) where the distribution of the hypocentres indicates a NE-dipping structure. After the addition of the portable network (Fig. 2), we can infer the position of the fault plane dipping 38° towards northeast (Fig. 3d). The inferred dip-angle is similar to the dip-angle of the northeast-dipping nodal plane of the moment tensor solutions (median value 39°; see Table 1). The northern cluster (Fig. 3; cross section A_1A_2) was activated one week after the M_w=6.3 event and the distribution of the events is not conclusive on the dip-direction of the seismic fault. The southern cluster (Fig. 3c; section C_1C_2) was active during the whole period, depicting a steeply dipping structure.

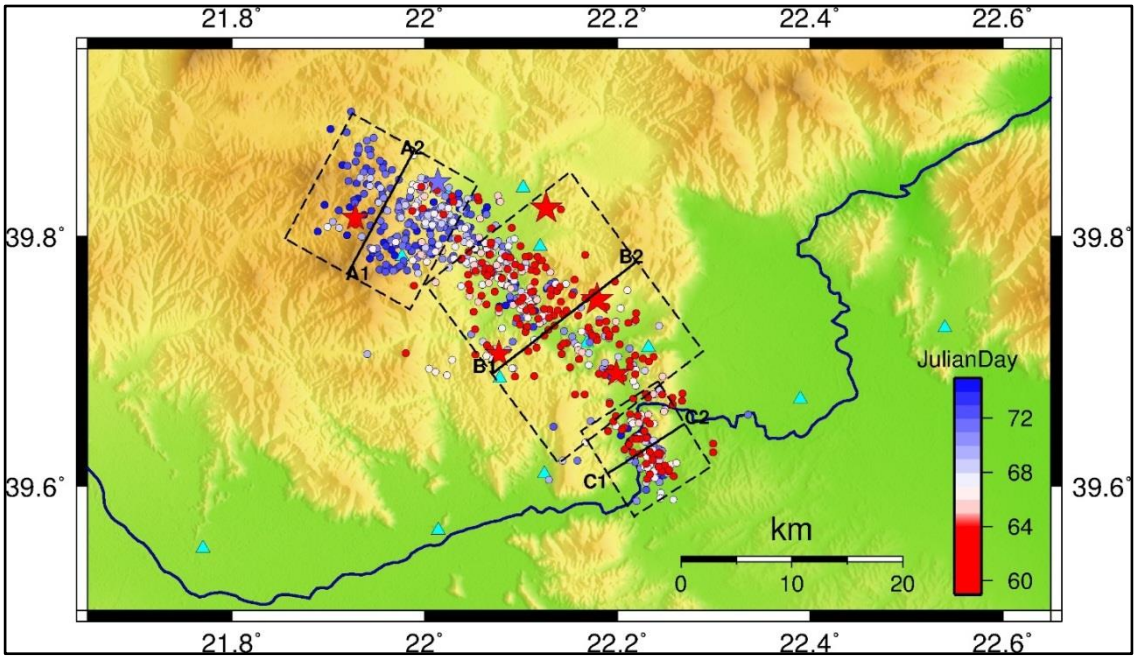

Fig. 2: Map of relocated seismicity. Epicentre colours are according to Julian date of occurrence. Sections A_1A_2, B_1B_2 and C_1C_2 are shown in Fig. 3. Cyan triangles indicate station locations.

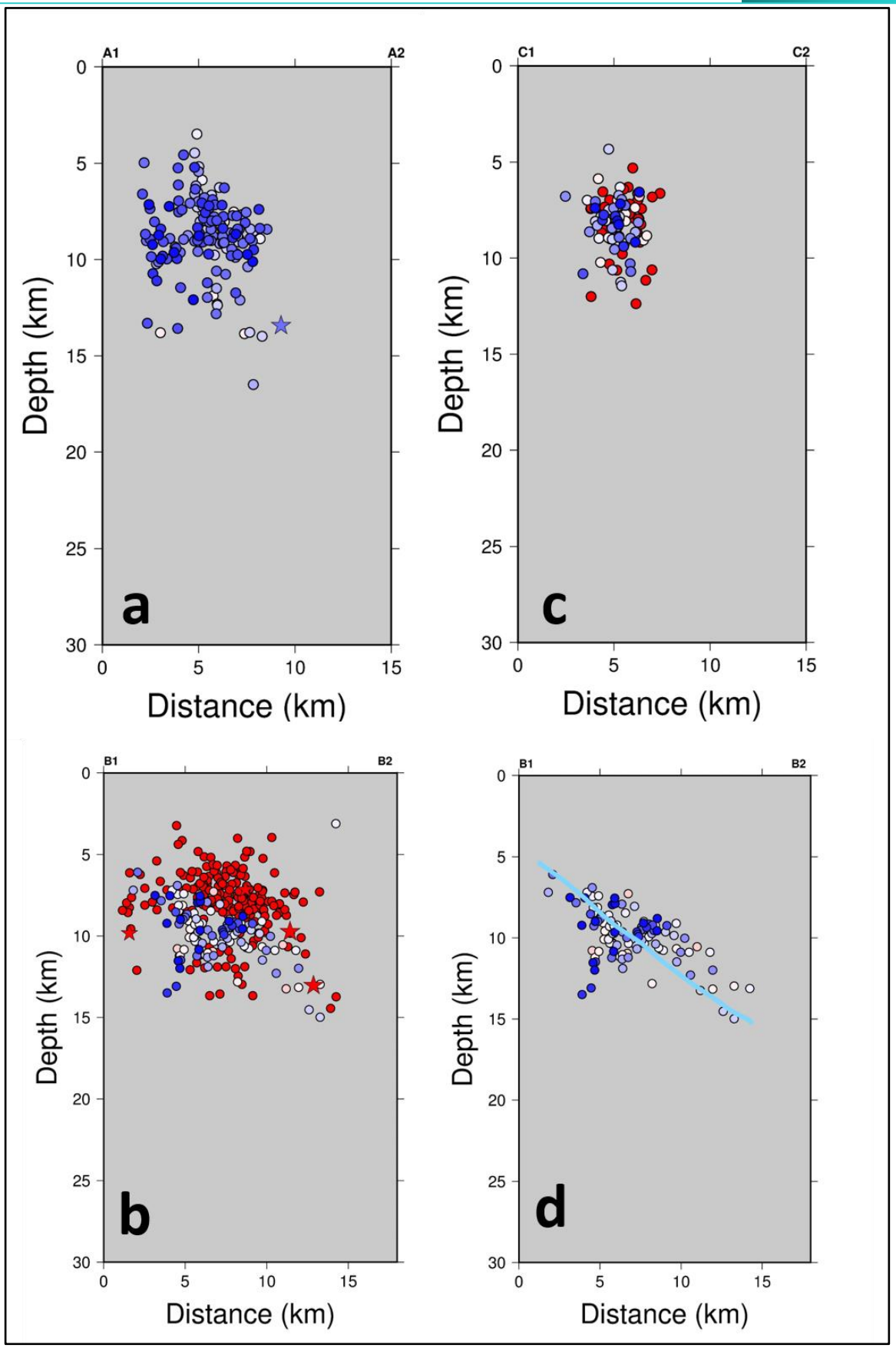

Fig. 3: Cross sections of relocated seismicity (a) to (c) corresponding to profiles A_1A_2, B_1B_2 and C_1C_2 respectively (see Fig. 2 for locations). Foci colours are according to Julian date of occurrence. Panel (d) displays the blue foci of (b) indicating aftershock

hypocentres from day 065 (March 6, 2021) onwards, together with an imaginary line showing the projection of the inferred fault plane with a dip-angle of 38°.

2.2. Computation of Focal mechanisms

The configuration of the regional HUSN seismic stations and accelerographs, allowed the computation of a large number of focal mechanisms using *P*-wave first motion polarities. This was possible especially after March 6, 2021 when the temporary local network was installed (Fig. 4). 5180 *P*-wave first-motion polarities were manually picked using Seisgram2K (Lomax, 2014). A total number of 408 focal mechanisms were determined using a grid search method applied on the first motion polarities (Kapetanidis, 2017). Out of the 408 solutions, herein, we present 22 focal mechanisms for events with M ≥ 4.0 as most representative of the rupture processes and afterslip. The stations positions on the stereo-net for the determination of the fault plane solutions by first motion polarities were determined using relocated hypocentres (where available) and the velocity model of Hatzfeld et al. (1997) by applying the TauP code (Crotwell et al., 1999). These focal mechanisms are shown in Fig. 4 according to their day of occurrence, indicating that 16 out 22 events with M ≥ 4.0 occurred with the first 48 hours from the first mainshock. Nearly all focal mechanisms exhibit normal kinematics or have a dominant normal dip-slip component. Oblique-normal and strike-slip focal mechanisms are also resolved, some being less constrained due to the unavailability of an adequate number of local stations until March 6, 2021. The parameters of 22 aftershocks are shown in Table 2 (and Table S2).

Table 2. Parameters of aftershocks with M≥4.0 determined with first polarities. See Table S1 for full parameters.

Year	Mo	Day	Hr	Min	Sec	Depth (km)	Mag	Strike (°)	Dip (°)	Rake (°)
2021	3	3	10	20	45.93	9.4	4.7	178.8	49.5	-43.8
2021	3	3	10	23	8.12	10.4	4.1	267.5	47.0	-139.7
2021	3	3	10	26	18.33	9.7	4.1	2.8	52.9	-37.8
2021	3	3	10	34	7.54	11.7	4.9	283.0	56.1	-148.8
2021	3	3	11	12	23.08	10.3	4.3	327.1	50.8	-41.6
2021	3	3	11	35	56.66	10.2	4.8	344.4	44.7	-87.5
2021	3	3	18	24	8.06	11.6	5.2	328.6	54.0	-34.7
2021	3	3	18	49	48.25	12.4	4.2	77.7	33.7	-92.0
2021	3	3	21	0	54.67	10.2	4.0	278.3	43.7	-145.3
2021	3	4	2	43	37.77	11.6	4.0	349.1	36.7	-71.0
2021	3	4	9	36	15.37	13.2	4.4	130.9	48.0	-35.9
2021	3	4	18	45	26.58	11.9	4.1	242.0	51.4	-150.8
2021	3	4	19	23	50.99	11.6	5.0	248.8	41.9	-101.6
2021	3	4	19	31	31.96	11.5	4.2	125.0	52.7	-38.4

2021	3	4	20	3	8.11	11.1	4.2	331.7	53.5	-29.4
2021	3	5	9	59	58.96	15.1	4.2	86.0	41.7	-85.4
2021	3	5	10	1	14.49	10.3	4.2	294.8	36.0	-84.3
2021	3	6	16	36	17.51	11.6	4.1	356.0	65.3	-22.9
2021	3	6	19	47	39.76	9.6	4.1	3.7	47.9	-34.6
2021	3	11	14	19	40.4	6.3	4.0	124.4	46.9	-42.0
2021	3	15	15	43	37.71	8.0	4.3	263.2	24.5	-86.2
2021	3	21	17	15	54.04	8.8	4.1	287.5	42.3	-69.4

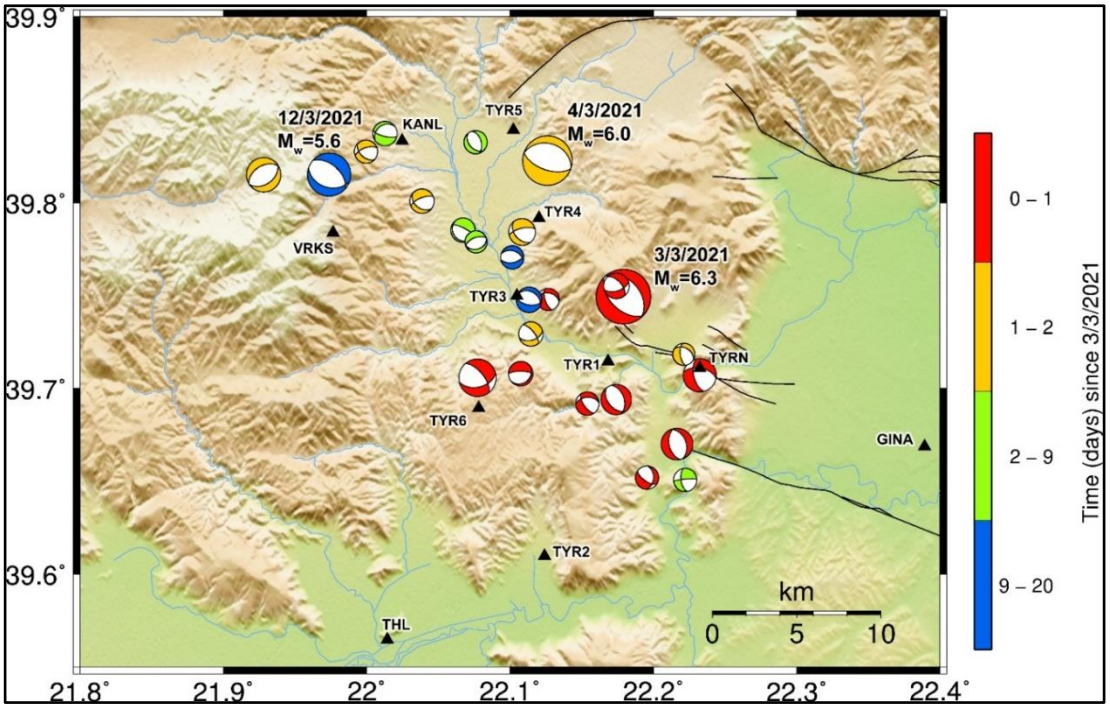

Fig. 4: Map showing the focal mechanisms of the three mainshocks (Moment Tensor solutions; median values from Table 1) and twenty-two major aftershocks with M≥4.0 (computed with the method of first motion polarities). Compressional quadrants are coloured according to the day of occurrence since 3 March 2021. Solid triangles indicate locations of the seismic instruments.

3. PROCESSING OF INSAR DATA - ANALYSIS OF INTERFEROGRAMS

InSAR is a technique of side-looking imagery collected by repeating passes of a radar satellite over an area. Since 1992, the technique it has been used to measure how much the ground surface has moved along the line-of-sight (LOS) between each pass of a satellite and can give vital information as to how much slip occurred on a fault. In the case of the Thessaly 2021 earthquakes preliminary field data indicate that the ruptured faults are "blind", i.e., they have no surface expression in terms of fault scarps (Ganas et al. 2021a; Valkaniotis et al. 2021). We used the ascending images acquired by the European Copernicus satellites Sentinel-1 (S1; C-band data) on the ascending tracks 102 and 175 and on the descending tracks 7 and 80. The

area of interest for InSAR is included within 21.7-22.5° in longitude and 39.5-39.9° in latitude. The geometrical characteristics of the S1 tracks are given in Table 3. Due to acquisition schedule and track geometry, the M_w=6.3 and M_w=6.0 earthquakes were captured only in ascending track interferograms as separate deformation events (Fig. 5; Fig. 6).

Table 3. Parameters of the four available S1 tracks.

Orbit	Ascending	Ascending	Descending	Descending
Track	102	175	7	80
Acq. time (UTC)	16:24	16:32	04:31	04:38
Incidence angle (°)	33.7274	41.5527	41.5469	36.8476
Incidence vector east, north, up	-0.537 -0.126 +0.832	-0.646 -0.151 +0.748	+0.646 -0.151 +0.748	+0.584 -0.137 +0.800

The interferograms (Fig. 5) were made using the SNAP v8.0 software (Veci et al. 2014). The digital elevation model (DEM) used for the processing is the Shuttle Radar Topography Mission (SRTM) 1 Arc-Second Global (doi: /10.5066/F7PR7TFT). During processing, the interferogram was formed by cross-multiplying the master image (the pre-event acquisition image) with the complex conjugate of the slave (the post-event image). The resulting phase represents the difference between the two images. Through the interferometric processing, we eliminate sources of noise, as much as possible, to isolate the remaining signal that is likely to be related to the ground displacement. We also enhanced the signal-to-noise ratio by applying the adaptive power spectrum filter of Goldstein and Werner (1998) with a coherence threshold of 0.4. For this sequence, the quality of the interferograms is good, both in terms of coherence and tropospheric noise.

The interferogram of the first event shows 13 fringes corresponding to ground deformation in the Damasi area (Fig. 5 left panel; see location of Damasi in Fig. 1). The interferogram of the second event shows 4 fringes corresponding to ground deformation in the Amouri area, about 10 km to the northwest (Fig. 6, middle panel; see location of Amouri in Fig. 1). All fringes correspond to motion away from the satellite (increase in the line-of-sight distance). The subsidence pattern is interpreted as result of co-seismic motion along two normal faults, running NW-SE and dipping to the northeast. The third event created a fringe pattern consistent with subsidence due to a south-dipping fault according to the shape and density of fringes (denser closer to fault's trace; Fig. 5 right panel). The InSAR results show that the Titarissios river valley and large areas to the west and SW of Tyrnavos moved roughly downwards.

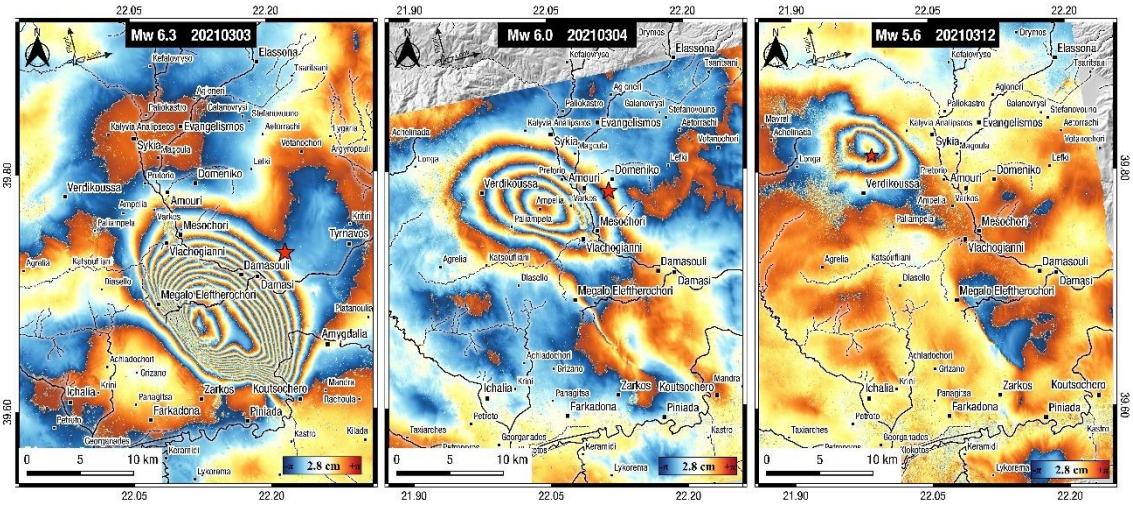

Fig. 5: Coseismic interferograms (wrapped phase; cropped swath) from Sentinel-1 SAR imagery pairs, for the three main events of the earthquake sequence. Left) Ascending track 102, February 25 – March 3, 2021. Middle panel) Ascending track 102, March 3 – March 9, 2021. Right panel) Ascending track 175, March 8 – March 26, 2021. The interferograms are draped over shaded relief. Red stars indicate epicentres of the three earthquakes. *A high-resolution version of this figure is provided in the supplement section of this article*.

We also used the LOS displacements from track 80 & 175 interferograms (March 2 – March 14, 2021) for decomposition into horizontal (East-West) and vertical displacement components. Decomposition processing combines the ascending and descending unwrapped interferograms (neglecting the contribution of the North-South displacement), using simplified geometry and the Sentinel-1 acquisition incidence angles (Wright et al. 2004; Dalla Via et al. 2012). These interferograms contain the cumulative deformation from all three main events (Fig. 6). Later interferograms show no significant deformation in the area. The majority of deformation occurs in the vertical component, with a maximum of 0.39 m of subsidence over the M_w=6.3 rupture plane, south of Damasi (Fig. 6 a & c). A small amount of uplift is observed in the area NE of Farkadona (Fig. 6a; up to 4 cm). The uplift might be attributed to the relative motion of the two fault blocks either side of the fault surface. In normal faulting the maximum surface displacement is manifested as subsidence of the hanging wall, with the footwall being uplifted but with less amounts (e.g., King et al. 1988). The small cumulative uplift of the Thessaly earthquakes is probably due to the blind character and intermediate dip-angle of the normal fault ruptures. A significant amount of E-W horizontal displacement (from +0.19 m to –0.1 m) is observed (Fig. 6 b & d), that is attributed to the crustal extension due to the normal fault ruptures.

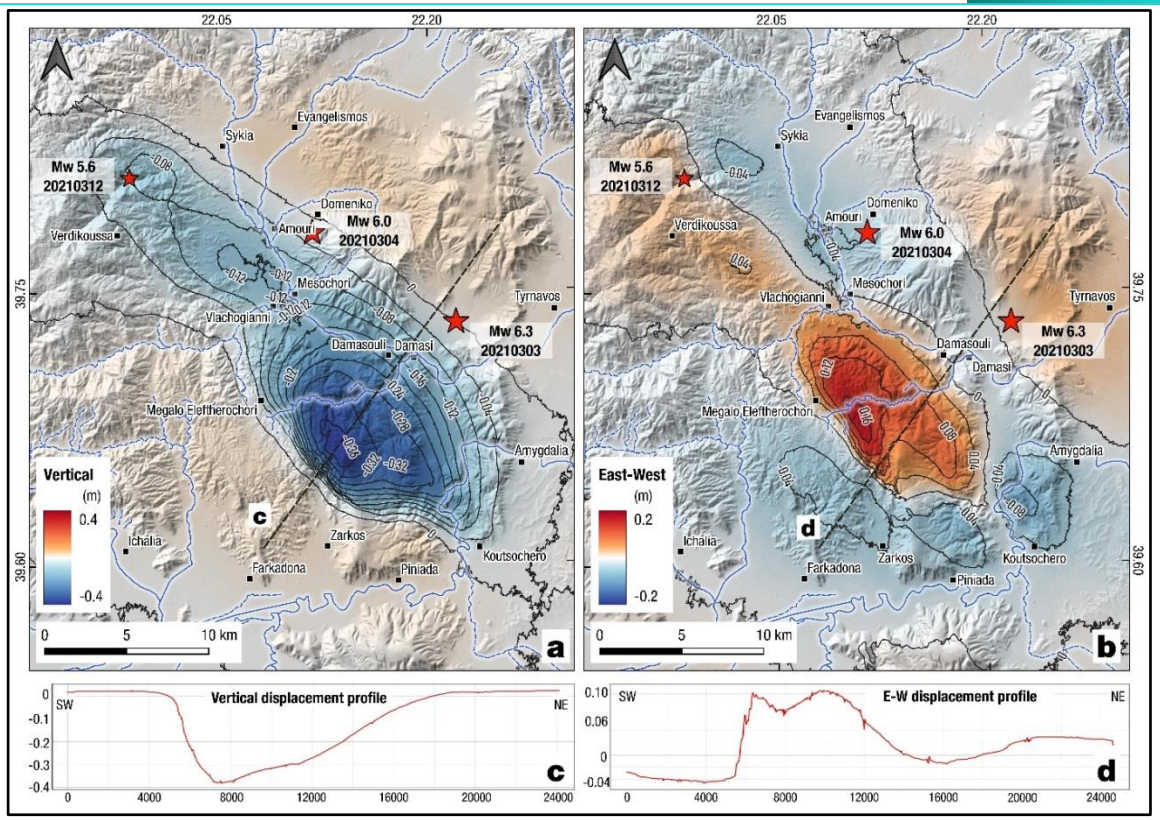

Fig. 6: InSAR displacement maps from the decomposition of Track 80 & 175 interferograms (2 March – 14 March 2021) a) vertical component b) east-west component with NE-SW oriented profiles in c) and d) respectively. Positive values (red colours) of E-W displacement show movement towards east. *A high-resolution version of this figure is provided in the supplement section of this article*.

4. CO-SEISMIC MOTION OF THE GNSS STATIONS

We analyzed dual-frequency GPS data of twelve (12) GNSS stations, all located in Thessaly. One station (KLOK) belongs to both NOANET (Ganas et al. 2008) and INGV (Fig. 1). It is equipped with a choke-ring antenna and its 10-yr long time-series analysis indicates a very stable behavior (Argyrakis et al. 2020). Two GNSS stations belong to AUTH-HERMES network (code name ELAS and LARM), five stations belong to Tree-URANUS (FAR2, KARD, LARI, PIRG and TRIK), two stations to METRICA- HxGN Smartnet (BELE, MURG) and two stations to JGC-net (KARJ and LARJ). The data (rinex v2.11 files) were processed with the Gipsy version 6.0 software of the JPL/NASA (Bertiger et al., 2010). For Tree-URANUS stations we processed data until April 25, 2021 while for METRICA-HxGN SmartNET stations until the March 31, 2021. Unfortunately, there were no data available for ELAS after March 5, 2021. The sampling interval was 30 s, and the data were collected on a 24-hour basis. We used the JPL final satellite orbits (flinnR) and clocks, absolute antenna calibration, random walk troposphere estimation and the FES2004 ocean loading model. We calculated the static offsets (and their uncertainties) for the three events (Table 4; Fig. 7 and

Fig. 8). The offsets indicate cm size motion mainly along the NE-SW direction. Station KLOK (Fig. 7) registered the largest displacements, as it moved 4.2 cm towards south and 3.1 cm towards west. In terms of Up-Down (vertical) displacement, we obtained no clear trends of co-seismic motion for the three events. We also processed in kinematic mode the high-rate data (1s sampling interval) of several stations, including station KLOK, using the CSRS-PPP SPARK, an online GNSS service developed by the Geodetic Survey Division of Natural Resources Canada. We present the results of the data processing for the March 4, 2021 shock in supplementary Fig. S2. Unfortunately, for the day of the March 3, 2021 earthquake station KLOK has a duration of observations of only 2:54:30 (hh:mm:ss), starting from 21:05:00.00 GMT.

The six best-constrained displacements of GNSS stations are shown in Fig. 7**.** The events of March 4, and March 12, 2021 are much smaller in size and do not contribute (they produce local InSAR fringes as seen in Fig. 5, but minor offsets were recorded in the intermediate and far field). The uncertainties on the displacements are (on average) 3 mm in east and north (~10% of a fringe). These values were used for assigning the zero of the interferograms. They were also used for the control of the prediction of the fault models. For modelling the fault parameters, InSAR is adequate for this seismic sequence while GNSS cannot constrain the models. There is no evidence of significant post-seismic displacement except some small displacements (below ¼ of a fringe) in the near field of the faults. Note that the co-seismic offsets on Fig. 7 appear smooth because we applied a Gaussian filter on the position time series; this filter reduces by a factor of two the signal-to-noise ratio of the time series, which is useful in case of small displacements.

In addition, in the time series of E, N coordinates plotted in Fig. 7, the secular velocities of the stations from Briole et al. (2021) have been subtracted. The station offsets are reported in Table 3 together with their modelled displacements according to the derived fault models (see section 5 below). The map of the horizontal displacement pattern is shown in Fig. 8. The horizontal displacement pattern is in agreement with the normal dip-slip kinematics of the rupture, i.e., axis of extension oriented ~NE-SW. We note that several stations located along strike (i.e., NW-SE), such as LARJ and LARM, recorded smaller displacements than stations such as KARD and TRIK, despite the latter being further to the epicentral area. This effect is due to the asymmetric elastic response of the crust during seismic faulting and it was also observed in the case of the Samos 2020 earthquake (Ganas et al. 2021b).

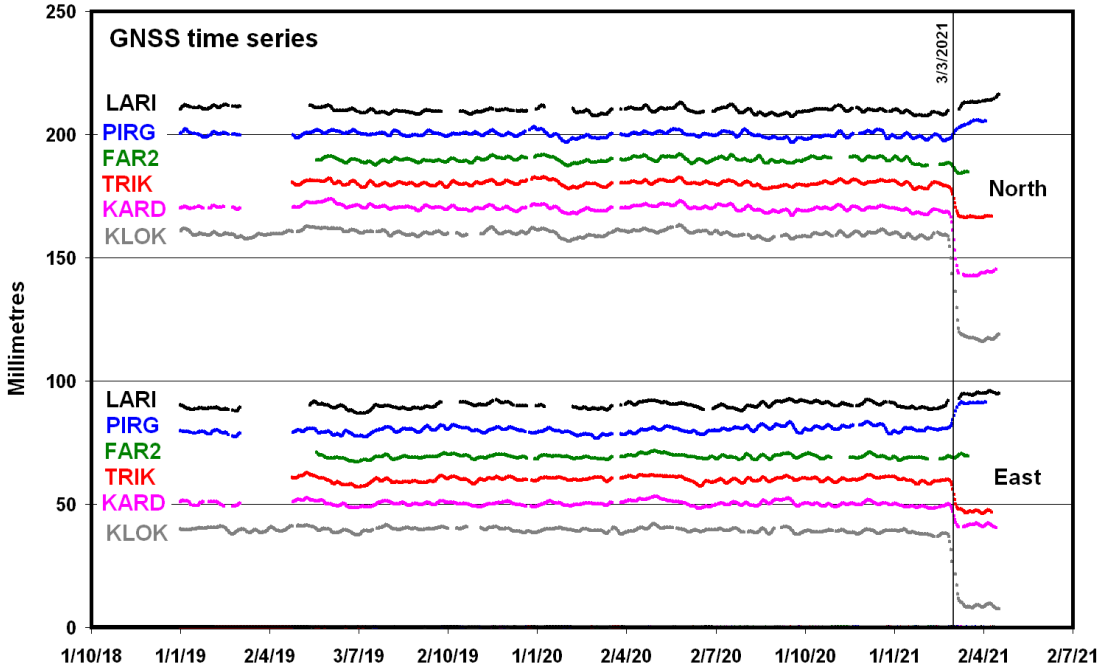

Fig. 7: Graphs showing position time series of GNSS stations in Thessaly (north and east components). The time-series have been offset for clarity on the Y-axis. Vertical line indicates the day of the 3 March 2021 event and marks the co-seismic displacements on six stations having the lowest uncertainties on the estimation of the co-seismic displacements. Station locations are in Fig. 8**.**

Table 4. Coordinates of the 12 GNSS stations, secular velocities (Briole et al. 2021), total displacement values (in mm; all three main shocks), total model values. The mean difference between observations and model is 0.8 cm, -1.6 cm, and -0.4 cm in east, north and up respectively. See Fig. 8 for station locations.

Station		Coordinates		Velocity ITRF2014		Total co-seismic motion			Model		
Code	**Owner**	**Long.**	**Lat.**	**vE**	**vN**	**East**	**North**	**Up**	**East**	**North**	**Up**
		°	°	mm yr^{-1}	mm yr^{-1}	mm	mm	mm	mm	mm	mm
BELE	Metrica	23.133	39.295	18.8 ± 0.5	0.3 ± 0.6	1 ± 1	0 ± 1	0 ± 3	0	0	0
ELAS	AUTH	22.206	39.892	22.7 ± 0.5	6.1 ± 0.6	12 ± 5	34 ± 5	0 ± 15	18	33	8
FAR2	Uranus	22.384	39.296	19.5 ± 0.8	3.1 ± 0.8	1 ± 1	-5 ± 1	8 ± 3	-1	-1	1
KARD	Uranus	22.082	39.470	20.4 ± 0.4	6.1 ± 0.5	-9 ± 1	-26 ± 1	3 ± 3	-10	-22	0
KARJ	JCG	21.745	39.355	n/a	n/a	0 ± 5	-5 ± 5	0 ± 15	-7	-8	2
KLOK	NOA/INGV	22.014	39.565	21.1 ± 0.2	6.6 ± 0.2	-31 ± 1	-42 ± 1	-2 ± 3	-32	-38	6
LARI	Uranus	22.400	39.637	20.5 ± 0.4	4.7 ± 0.4	5 ± 1	4 ± 1	3 ± 3	5	5	4
LARJ	JCG	22.413	39.622	n/a	n/a	3 ± 5	1 ± 5	1 ± 15	3	4	4
LARM	AUTH	22.388	39.614	21.3 ± 0.2	5.3 ± 0.3	-1 ± 2	3 ± 2	6 ± 6	0	6	3
MURG	Metrica	21.554	39.739	21.7 ± 0.4	7.9 ± 0.4	-1 ± 2	1 ± 2	0 ± 6	-4	-2	1
PIRG	Uranus	22.589	39.919	22.4 ± 0.4	6.0 ± 0.4	11 ± 1	5 ± 1	1 ± 3	11	8	0
TRIK	Uranus	21.798	39.555	20.0 ± 0.6	7.4 ± 0.8	-13 ± 1	-13 ± 1	5 ± 3	-14	-12	0

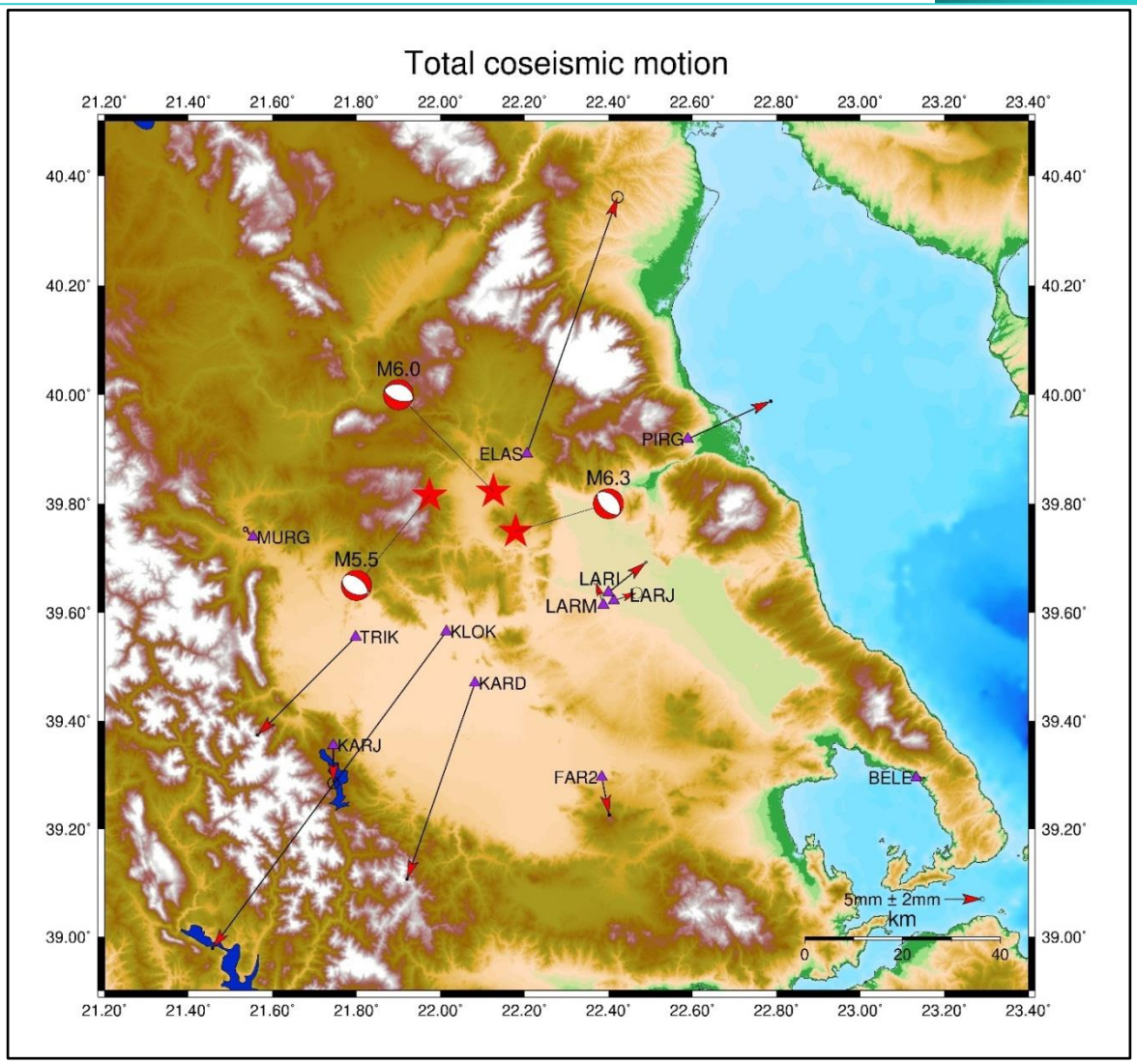

Fig. 8: GNSS total displacement map showing also topography/bathymetry, the focal mechanisms (beachballs; compressional quadrants in red) and the epicentres of the Thessaly 2021 earthquakes. Triangles indicate permanent GNSS station locations. Vectors indicate the horizontal displacement of GNSS stations with 67% confidence scaling. Notice the large displacements obtained for stations located normal to the strike of the seismic faults.

5. INSAR DATA INVERSION - FAULT MODELS

In the Damasi earthquake sequence there are three main events, that occurred on March 3 (M_w =6.3), March 4 (M_w=6.0) and March 12, 2021 (M_w=5.6). In our inversion models, we use as initial values for the angles (azimuth, dip) the median angles of the available focal mechanisms (Table 1). The choice of the dip-angle is also justified by the results of seismicity relocation, as we infer a 38°-dipping fault plane towards the NE (Fig. 3d). Ten (10) interferograms are used and inverted to estimate the parameters of the faults responsible for the earthquakes (Table 4). The coherence of those interferograms is, on average, outstanding. Weather during the period of interest was most of the time cold and dry and therefore the tropospheric effects

are very small. The ground surfaces are partly rocky, which also greatly contributes to the overall coherence. In each of the ten interferograms, we pick the fringes where they are visible and unambiguous. The fringe number zero (0) is accurately determined on the basis of the displacements recorded at the GNSS stations (see section GNSS above). Then, this zero is controlled and fine-tuned during the modelling/minimisation process. We also made several post-seismic interferograms, until May 1, 2021, and we have seen that there is almost no post-seismic deformation, even in the near field. The post-seismic displacements are below the 7 mm level (quarter of fringe) in the near field and below the 1 mm level at the GNSS sites.

Table 5. Interferograms used for the modelling of the faults. Events: 1 is for March 3 (M_w =6.3), 2 if for March 4 (M_w=6.0), 3 is for March 12, 2021 (M_w=5.6). The bias is the value (in mm) of the offset applied to the picked fringes to minimize the residuals in the modelling. Tracks A102 and A175 are ascending, D007 and D080 descending.

Track	**Start**		**End**		**Picked points**	**r.m.s. fit**	**bias**	**Event**
	Date	***Orbit***	***Date***	***Orbit***		***mm***	***mm***	
A102	19/02/21	25678	03/03/21	25853	453	40.6	6	1
A102	03/03/21	25853	09/03/21	36924	106	7.4	14	2
A102	25/02/21	36749	09/03/03	36924	783	41.9	7	1+2
A175	24/02/21	25751	08/03/21	25926	834	42.4	6	1+2
D007	03/03/21	36829	09/03/21	25933	376	42.1	-9	1+2
D080	24/02/21	36727	08/03/21	36902	490	37.2	-5	1+2
A102	09/03/21	36924	15/03/21	26028	45	7.7	9	3
A175	08/03/21	25926	14/03/21	36997	31	4.3	-15	3
D007	09/03/21	25933	15/03/21	37004	48	5.1	3	3
D080	08/03/21	36902	14/03/21	26006	51	6.2	0	3

Each earthquake is supposed to correspond to a homogeneous dislocation on a rectangular fault buried in an elastic half-space. The formalism used is the one established by Okada (1992). The inversion is made with the method developed by Briole et al. (1986) using the code *Inverse6* (Briole, 2017). For the first and second events, only track A102 contains those earthquakes separated from the others. We inverted the corresponding interferograms (parameters in Table 5) to estimate a first model for each of those events. Then, we combined

the two events and made a joint inversion of the four interferograms available on the four tracks to fine-tune the parameters of the two faults. Although mixing the two faults in one single inversion may reduce the discrimination potential of the inversion, this is balanced by the fact that the combination of the four tracks allows to assess in a more robust manner the zero bias of the four sets of picked fringes (column bias in Table 5). This robustness is enhanced by the fact that there are ascending and descending data which greatly stabilizes the inversion and provides robustness.

The parameters of the best-fitting models are in Table 6. The modelled fault sources are shown in Fig. 9 as shaded rectangles. The fault sizes are: 9.6 km long by 10.5 km wide (March 3 event), 11.9 km by 4.0 km (March 4 event) and 4.3 km by 5.5 km (March 12 event), respectively. The longer fault size of the March 4 event is due to the particular rupture characteristics; the March 3 event occupied a larger rupture area due to most slip occurring down-dip of the fault plane.

Table 6. Source Parameters of the fault models based on the inversion of geodetic data.

Parameter		**Unit**	**March 3 event**	**March 4 event**	**March 12 event**	**Notes**
Centre of upper edge	Longitude	°	22.134 ± 0.010	22.066 ± 0.010	22.002 ± 0.010	
	Latitude	°	39.665 ± 0.010	39.760 ± 0.010	39.827 ± 0.010	
	Up	km	3.0 ± 1.0	4.2 ± 1.5	1.3 ± 1.0	
Azimuth		°	318	298	108	Not inverted (used values from seismology)
Dip angle		°	39	36	40	
Length		km	9.6 ± 1.0	11.9 ± 1.5	4.3 ± 1.0	
Width		km	10.5 ± 2.0	4.0 ± 1.0	5.5 ± 1.0	
Strike slip		m	0.082	-0.021	0. (not inverted)	Positive = left lateral
Dip slip		m	1.173	0.591	0.25	Positive = normal
Geodetic moment		N m	$3.56\ 10^{18}$	$0.84\ 10^{18}$	$0.18\ 10^{18}$	

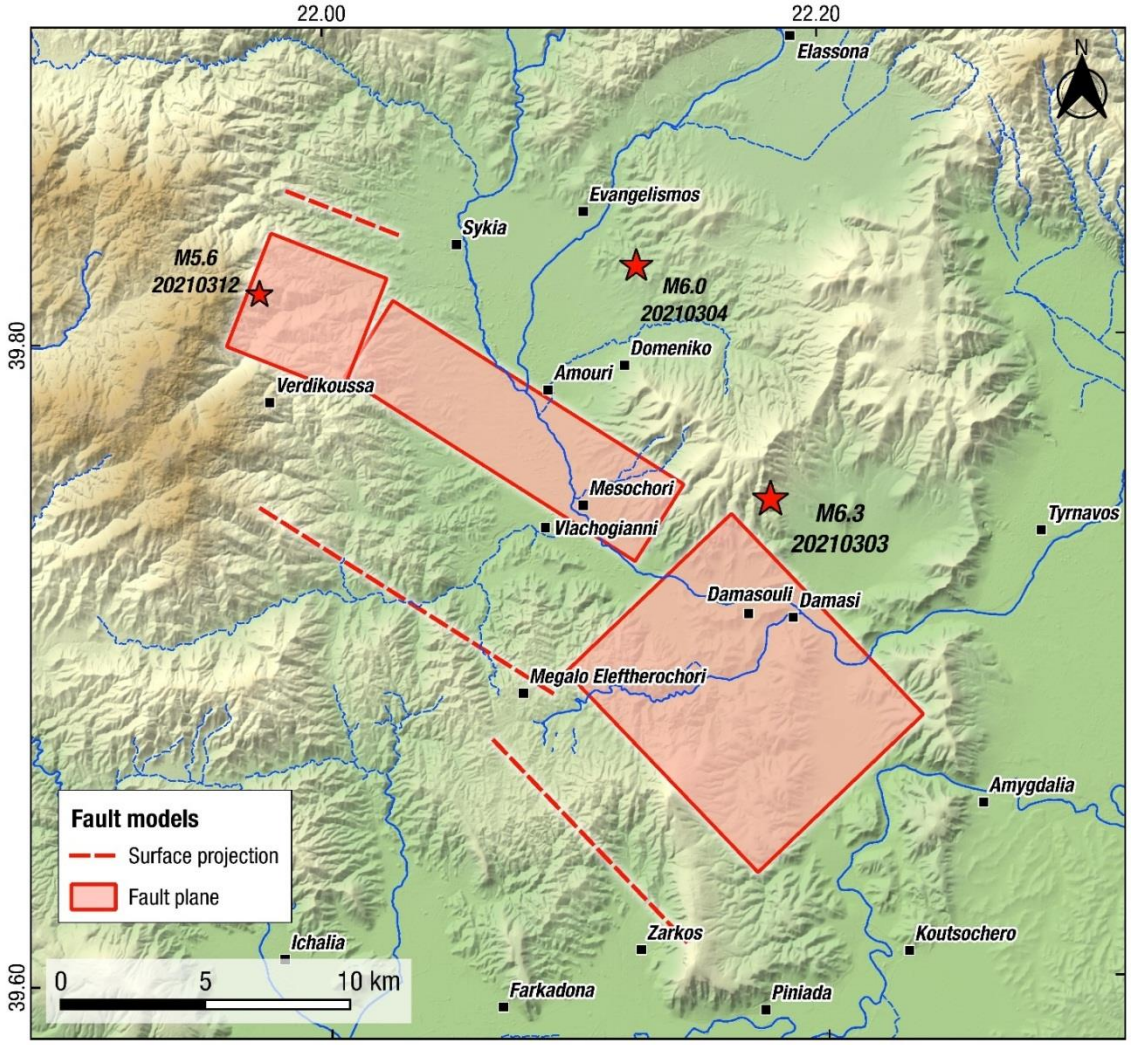

Fig. 9: Surface projection of the faults (shaded rectangles) of the three events. Dashed red line is the intersection of the fault plane at the surface (when projected up-dip). *A high-resolution version of this figure is provided in the supplement section of this article*.

6. GEOLOGICAL AND MACROSEISMIC OBSERVATIONS

6.1 Geological effects

Following the M_w=6.3 earthquake of March 3, 2021 the most prominent earthquake environmental effects were the widespread liquefaction phenomena and lateral spreading that was triggered over Titarissios and Pinios river valleys (Fig. 10; Valkaniotis et al. 2021). The Titarissios and Pinios basins have Pliocene-Quaternary fluvial and lacustrine sediments deposited directly on the metamorphic basement (Caputo et al. 2021). During post-earthquake surveys, we mapped more than 500 sites with liquefaction fissures and craters and lateral spreading deformation/cracks. A number of sites with high density of liquefaction fissures were surveyed by the UAS (Unmanned Aircraft System) model DJI 4 Pro V2.0. Co-seismic

interferograms revealed two large areas, along the Titarissios river valley to the north and Pinios river valley to the south (orange-shaded polygons in Fig. 10), with very low to no coherence. We suggest that lack of coherence in those areas is related to widespread surface deformation and change due to liquefaction. In addition, low InSAR coherence over Titarissios valley suggests repeated liquefaction and lateral spreading during the second (M_w=6.0) earthquake on March 4, 2021. Careful examination of post-earthquake Sentinel-2 optical imagery (10-m ground resolution) revealed a number of sites with evidence of liquefaction fissures and craters. Our field survey lasted during the period March 3 – 15, 2021 and validated these satellite observations. The vast majority of liquefaction and lateral spreading surveyed sites are found along the Titarissios valley from Amouri to Damasouli villages (Fig. 9 & 10), and Pinios river valley from Farkadona to Koutsochero (Fig. 9 & 10). Liquefaction fissures and craters were more prominent inside the Pinios river valley, due to the presence of finer fluvial sediments, while the Titarissios valley has a dominance of coarser-grained material deposited on the flood plain (gravels, coarse sand). Preliminary examination of local palaeogeography and surficial geology revealed a possible correlation between liquefaction manifestations and fluvial geomorphology – palaeochannels (Valkaniotis et al. 2021). Witness reports from local residents describe the strong manifestation of sand and water ejection immediately after the M_w=6.3 earthquake. We suggest that localised ground deformation and displacement due to lateral spreading is responsible for a large number of geotechnical failures, mostly related to bridge and road embankments.

Landslides from the March 2021 earthquake sequence were rather limited, despite the magnitude and shallow crustal depth of the events. We mapped about 40 sites of landslides and rockfalls around the epicentral area (Fig. 10), from field observations and post-earthquake Sentinel-2 optical imagery (March 4 and March 14, 2021 acquisitions). Apart from a series of debris and avalanches in the steep gorge of Pinios west of village Amygdalea (Fig. 9 & 10), and a number of large boulders uphill the Zarko village, most locations involved landslides and rockfalls of small extent and size. A small number of ground cracks were also surveyed around the epicentral area (Fig. 10). Most of those might be related to local gravitational phenomena but without solid evidence to suggest a clear relation with larger slides or lateral spreading. We found two localities that deserve more attention. First, ground cracks were observed and surveyed at two locations along the western sector of the Tyrnavos fault trace (red triangles in Fig. 10; Caputo, 1993), north of village Damasi, immediately after the M6.3 earthquake (on the afternoon of March 3, 2021). The cracks are oriented approx. N308°E and show an opening of less than 1 cm. However, these cracks show no vertical offset. Therefore, the cracks may be related to triggered shallow slip along a section of the Tyrnavos fault by the March 3 rupture or to ground failure due to strong ground motion as this locality is situated above the rupture plane (see its extent in Fig. 9). More importantly, two sets of ground

fractures were surveyed north of village Zarko, with an average orientation of N355°E. These tensional cracks coincide with a zone of co-seismic and post-seismic secondary slip mapped with InSAR (location 4 in Fig. 10; Fig. 14d). This deformation zone possibly coincides with the surface projection of the M_w=6.3 rupture plane (see dashed red line in Fig. 9) and we examine the data in section 7.3 below.

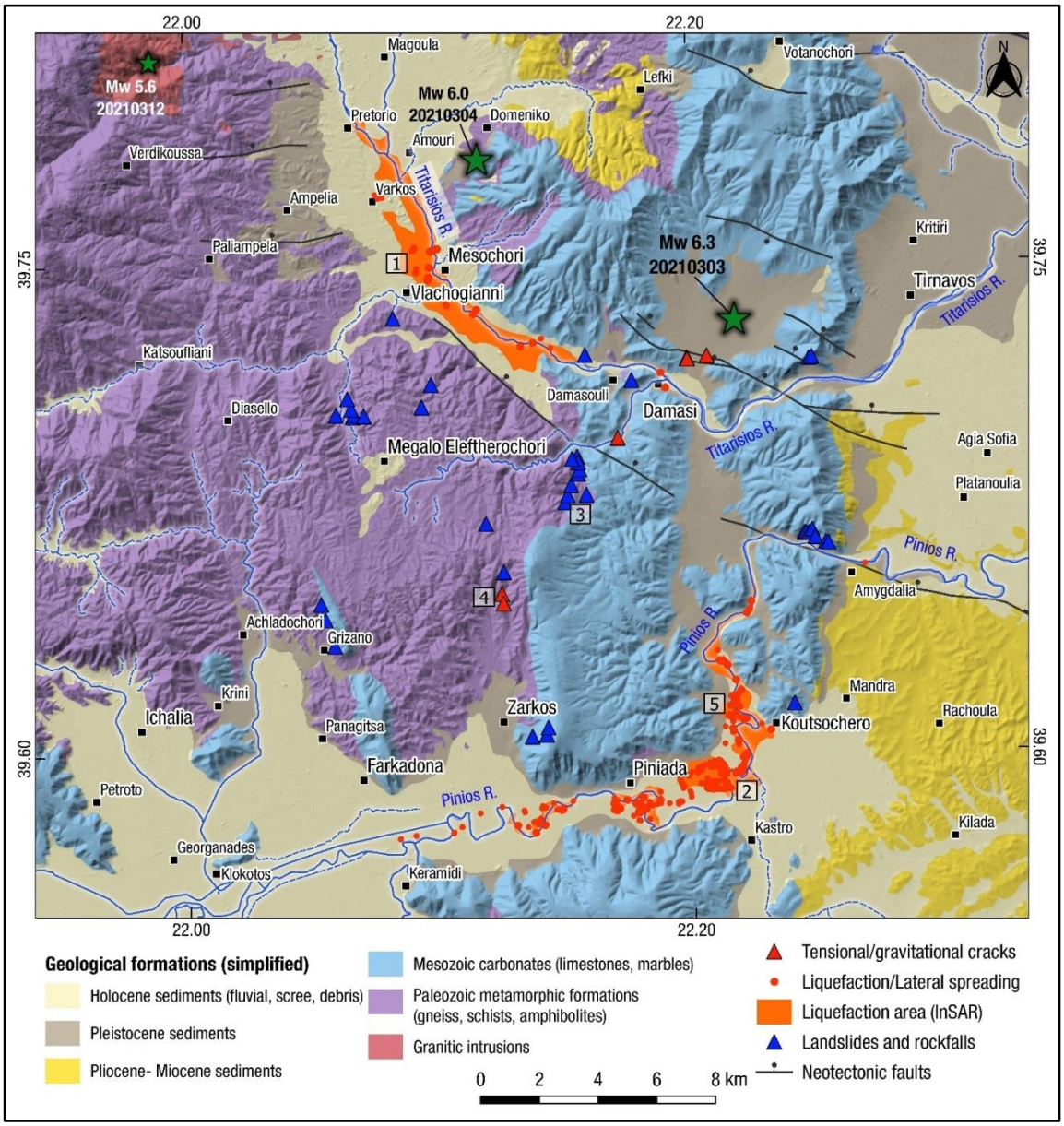

Fig. 10: Overview of field observations of the geological/environmental effects from the March 2021 earthquake sequence. The majority of earthquake effects are found within an area of approximately 20 km x 20 km. Epicentres of the main three events are shown with green star symbols (source AUTH). Simplified geological map is based on IGME maps. All field data were collected by SV, GP and AG during March 3-15, 2021. Simplified geology from the IGME map sheets compiled by Migiros (1985), Plastiras (1985), Stamatis (1987), Triantafillis (1987) and Vidakis (1998).

Fig. 11: Field photographs showing a & b) Liquefaction fissures with ejected sand in Titarissios river valley c & d) Liquefaction fissures with ejected sand in Pinios river (Piniada valley) e & f) Large sand boil craters in Pinios river sediments g) distributed deformation and ground cracks from lateral spreading in Pinios river terrace near Piniada h) localised graben structure in the head scarp of a lateral spreading (Pinios river valley north of Koutsochero). See village locations in Fig. 10.

Fig. 12: Field photographs showing a) Upthrown rocks in a gentle slope near Tsouma Monastery (Location 3 in Fig. 10) b) Rockfalls and debris along a mountainous road south of Damasi c) Rockfalls and wedge chips in a road cut north of Grizano d) Tension cracks north of Zarko, possibly along the surface projection of the M6.3 rupture plane (Location 4 in Fig. 10) e) Lateral spreading phenomena along the Pinios river valley, north of Koutsochero. f) Liquefaction at the base of the bridge pillars. Larissa – Trikala new highway bridge over Pinios river, west of Koutsochero (location 5 in Fig. 10).

6.2 Macroseismic observations and structural damage

The strong earthquakes and aftershocks of March 2021 revealed the seismic vulnerability of the critical infrastructure (e.g., bridges) and building stock in Thessaly. A summary of the structural damage observations obtained from the earthquake engineering field survey are presented below.

Bridges: Damage to bridges was reported and observed after the first earthquake on Wednesday 3 March 2021. Operation of the bridges that suffered damages around the epicentral area was suspended for a few hours after the earthquake, until an evaluation of their structural performance was performed by state engineer teams. The majority of the bridges suffered only surficial or minor structural damages, rapidly repaired during the first days after the main earthquake. The Titarissios bridge near Mesochori (Fig. 10) suffered moderate damage, due to extensive lateral spreading and liquefaction on its embankment, and remained closed to traffic (as of 30 June 2021). Most of the damage in bridges encountered in the epicentral area can be attributed to foundation and large displacements of their structural components due to lateral spreading / liquefaction along Pinios and Titarisios rivers (Fig. 11; Fig. 12).

Reinforced concrete (RC) buildings: The response of reinforced concrete buildings when subjected to earthquakes is highly dependent on the distribution of stiffness and mass in both the horizontal and vertical direction. RC buildings designed as per the more recent Greek seismic codes and the Eurocodes didn't experience any significant damage. Some damage occurred mainly to non-structural elements of RC buildings such as in-plane and out-of-plane failure of infill panels (Fig. 13a). In some cases, damages were observed in open ground floors (*pilotes*) in RC buildings designed and constructed before 1985.

The lack of shear reinforcement accompanied with loss of stiffness due to open ground floors led to shear failures of columns and beam to column joints. Lack of appropriate shear links resulted in buckling of the longitudinal rebars of the columns. The strong beams remained undamaged while severe damage and plastic hinges developed at the top of the columns (Fig. 13b). In other cases, and where not enough reinforcement was installed in shear walls, diagonal shear cracking occurred.

Masonry buildings: A significant amount of unreinforced masonry buildings can be found in the villages of the epicentral area. Such buildings can be grouped into three main categories: a) residential; b) schools; and c) churches. Masonry is a brittle and anisotropic material which is strong in compression and weak in tension. Masonry buildings were made of masonry units

(e.g., bricks, stones, concrete blocks, adobe) bonded together with or without mortar joints. At low levels of stress, masonry is behaving as a linear elastic matter. Its behaviour is becoming highly non-linear with the development of cracks and the redistribution of stresses in the uncracked regions during ground vibrations. Cracks in masonry buildings may open and close according to the type of stresses applied to them. Typically, cracks greater than 0.2 mm in width are visible to the naked eye. If such cracks open and propagate through the structure, they may reduce its load-carrying capacity and could lead to collapse. The preliminary damage assessment presented here is based on the patterns of cracks and dislocation observed on the exterior of the buildings, since access to the interior was not allowed at the time of the visit.

Residential masonry buildings: Typical domestic masonry buildings in rural areas of Thessaly are single- or two-story ones. These were constructed with uncoarsed rubble (irregularly shaped) unreinforced stone masonry and multi-leaf walls. The thickness of the walls is usually 0.5 m, but in some cases, it can be larger and even up to 1 m. Also, residential buildings in the region are characterised by large openings with or without lintels above them. In most cases, such buildings were constructed before 1959 and thus without any seismic provision. Since these buildings were not built using modern building codes, they suffered significant damage and even collapse. The extent of damage varies from one building to the other and from region to region.

Field investigations carried out after the earthquake demonstrated that poor construction techniques, poor material quality of multi-leaf masonry walls and lack of maintenance was the main reason for their structural damage, which in cases led to complete collapse. In particular, pounding, diagonal shear cracking in piers between window openings, delamination of the outer leaf of the walls as well as out-of-plane partial or complete collapse of walls observed in most of the residential unreinforced masonry buildings in Damasi and Mesochori (see Fig. 13d - 13f). In such places, walls were constructed with mud mortar, which is of very low strength and has very low resistance to humidity.

Another reason for the development of such out-of-plane failures are the absence of horizontal binding elements and, inadequate connections at wall intersections. Also, many of the buildings in the region lacked stiff in plane diaphragms at the floor and roof level. So, during earthquake, each of the load bearing walls acted independently in the in-plane and out-of-plane direction under the which led the buildings to collapse (See Fig. 13f).

Schools: Damages observed in school buildings made of masonry in Thessaly follow the typical damage typology of the masonry residential buildings. Significant damage occurred at the exterior and interior walls of the school of Damasi which was built in 1938 and is shown

in Fig. 13g. During the earthquake, parts of the load bearing walls of the building failed in the out-of-plane direction while some in-plane diagonal and bi-diagonal shear cracks and out-of-plane failure occurred at the piers. In the interior of the building, major diagonal shear cracks at the masonry walls as well as non-structural damages such as delamination of coating and overturning of chairs, desks and equipment occurred. The structure has been characterised as unsuitable and has been demolished.

Churches: The earthquake of March 3, 2021 proved to be particularly devastating for religious buildings made of masonry in Thessaly. Although religious buildings usually consist of well-constructed material, many of them do not meet any seismic standards since they were constructed over 80 years ago and were eventually deemed dangerous or unsuitable for immediate use. The damages in churches that were observed are typical for stone constructions and include: damage at their upper part in the system of arches and domes which are anyhow vulnerable to earthquake action, cracks in the corners of the windows and doors openings, cracking and rotation of bell towers which in cases led to their collapse (Fig. 13h). Temporary measures were installed in many churches with damages a few days after the earthquake to avoid further damage and collapse due to aftershock activity.

Fig. 13: a) Detachment of infill wall from RC frame in Damasi; b) Lack of proper detailing in an open ground floor in Damasi; c) Cross-section of a typical multi-leaf wall; d) Delamination of the outer leaf of the wall in a domestic building in Damasi; e) Out-of-plane collapse of masonry walls in Damasi; f) Out-of-plane collapse due to poor connection between the roof and masonry walls in Damasi; g) Damages in the School of Damasi; h) Out of plain failure of St Nickolas Church in Koutchochero.

7. DISCUSSION

7.1. Domino-style Faulting and Coulomb stress Transfer

Static stress changes due to the mainshock have been computed using the Coulomb failure criterion (CFF or Coulomb failure function; King et al., 1994; Ganas et al. 2006b; Toda et al., 2011; Taymaz et al. 2021), assuming the source parameters listed in Table 6 and effective coefficient of friction μ'=0.4. Most active faults in the north Thessaly area strike ±30° with respect to the seismic fault of the 3 March 2021 event (Fig. 1 and Table 1), so it is reasonable to model static stress transfer on receiver faults with similar kinematics as those of the first two events (Fig. 14)**,** but also on faults optimally oriented to the regional stress field (~N184°E; Kapetanidis and Kassaras, 2019; see Fig. S3 for a map of static stress transfer on optimal fault planes). As in section 5, we assume that failure of the crust occurs by shear, so that the mechanics of the process can be approximated by the Okada (1992) expressions for the displacement and strain fields due to a finite rectangular source inside an elastic, homogeneous and isotropic half-space. The ΔCFF results presented in Fig. 14 at depth of 9 km, i.e., the average depth of aftershocks (see Fig. 3; also Fig. S4) show: a) positive stress changes (loading) along strike of the March 3, 4 and 12, 2021 seismic faults, of the order of several bar and b) negative stress changes (stress shadows) across the strike of faults. Therefore, it is suggested that this stress transfer model explains well the on- and mainly off-plane distribution of aftershocks at that depth.

Moreover, this sequence increased Coulomb stress on segments to the northwest and southeast of the ruptures, which are potential sites of future earthquakes (with similar kinematics), and decreased Coulomb stress orthogonally to the rupture plane. We suggest that the M_w=6.3 earthquake promoted failure at the crustal volume of the M_w=6.0 earthquake which struck 32 hours later. It is notable the absence of aftershocks inside the area of the northern shadow (blue lobe), around the town of Elassona. We also find that the stress transfer results explain the cascade-type triggering of the three shocks in a domino-model of earthquake occurrence, from SE (Damasi area) towards the NW. The triggering pattern is probably influenced by the rupture kinematics of the first event, with a large slip patch located close to the SE tip of the second fault. A SE to NW directivity could have possibly resulted in a cascading (domino) rupture of the neighbouring segment (March 4 fault) which in turn triggered slip on the isolated segment of the March 12, 2021 event (see Fig. 15 for a faut segment map).

We note that the Larissa active fault has been loaded with stress transferred (red lobe in Fig. 14a) after the first event; therefore, it has been brought closer to failure (see the map in Fig. S3). Furthermore, a small cluster of aftershocks is observed directly SE of the main rupture,

within the ΔCFF +1.0 bar lobe; however, this activity lies on the footwall of NNE-dipping Larissa fault. We interpret that this indicates a likely smaller, unmapped structure. It is also very interesting, that there is no activity along the Larissa fault proper which is located in ΔCFF red (stress-loaded) areas (Fig. 14).

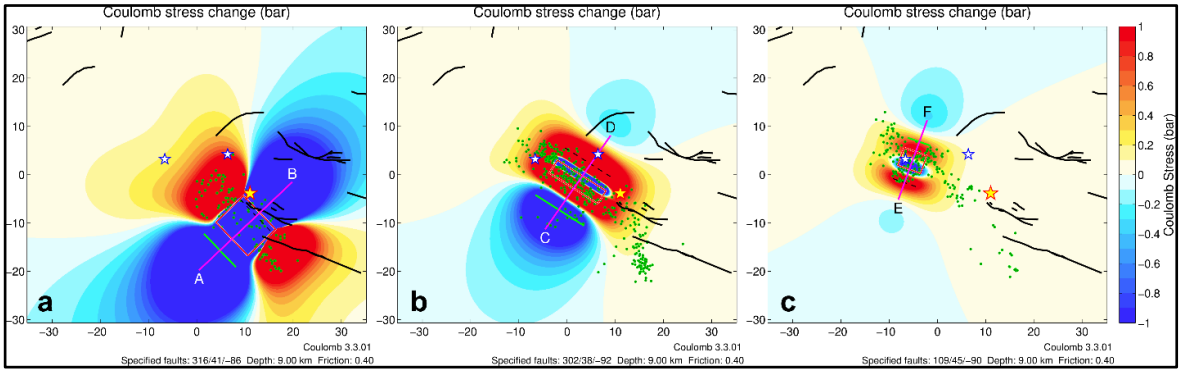

Fig. 14: Coulomb stress changes (ΔCFF) at 9-km depth (roughly corresponding to the average depth of aftershocks) associated with the northern Thessaly earthquakes a) after the 1st event, b) after the 2nd event and c) after the 3rd event, respectively. The palette of Coulomb stress values is linear in the range −1 to +1 bar. The stress change has been computed for receiver faults with the same kinematics as the source models (see Table 6). Red rectangle is the surface projection of the rupture plane, and green line is its surface trace (projected up-dip). Green circles are relocated aftershocks for the periods of a) March 3 - March 4, 2021 17:41 UTC b) 4 March, 18:38 UTC – 12 March, 12:57 UTC and c) 12 March, 12:57 – 16 March 2021. Profiles A-B, C-D and E-F are used for the ΔCFF cross-sections of Fig. S4. Colour scale in bar (1 bar = 0.1 MPa); blue areas: ΔCFF unloading (relaxed); red areas: ΔCFF loading.

7.2 Active faulting in northern Thessaly and the 2021 seismic faults

Clustering of earthquakes along neighboring fault segments in Greece that ruptured in a domino pattern involving two or three mainshocks has been observed in 1894 (Atalanti; Ganas et al. 2006), 1978 (Mygdonia; Soufleris et al. 1982; Tranos et al. 2003), 1981 (Alkyonides; Jackson et al. 1982), 2014 (Cephalonia; Valkaniotis et al. 2014; Lekkas and Mavroulis, 2016) among other cases. In Thessaly, there was a cluster of strong events during the period 1954-1957 (Pavlides, 1993; Papadimitriou and Karakostas, 2003) along normal faults, oriented ~E-W. In Northern Thessaly there are no data (at least instrumental) indicating earthquake clustering, so the 2021 seismic sequence was unprecedented.

The activation of three blind faults during the March 2021 seismic sequence indicates the continuity of active structures west of the known active faults of Northern Thessaly, i.e., the Rodia, Tyrnavos and Larissa faults (Fig. 15). The inversion modelling of InSAR data suggests the activation of intermediate-angle normal faults, previously unknown, or likely exploiting

crustal structures inherited from previous events (Tolomei et al., 2021). The lack of fault characterisation in this area in Greek active fault databases (Caputo and Pavlides, 2013; Ganas, 2020) probably reflects the subtle nature of surface deformation without the development of large basins and well-defined erosional features. The intermediate-angle rupture planes of the 2021 seismic faults also do not contribute to the considerable build-up of footwall topography, either. This intermediate-angle geometry of the 2021 seismic sources probably continues towards the west (i.e., between Trikala and Deskati; Fig. 1; Antihassia mountains) as the subdued landscape is dominant; however, the strain rates are comparable (~30 ns/yr). Early InSAR studies (Salvi et al., 2004; Ganas et al. 2006) mapped surface deformation on the mountains west of Elassona and Tyrnavos, however, no GNSS stations were in operation at that time, so as to validate the SAR results.

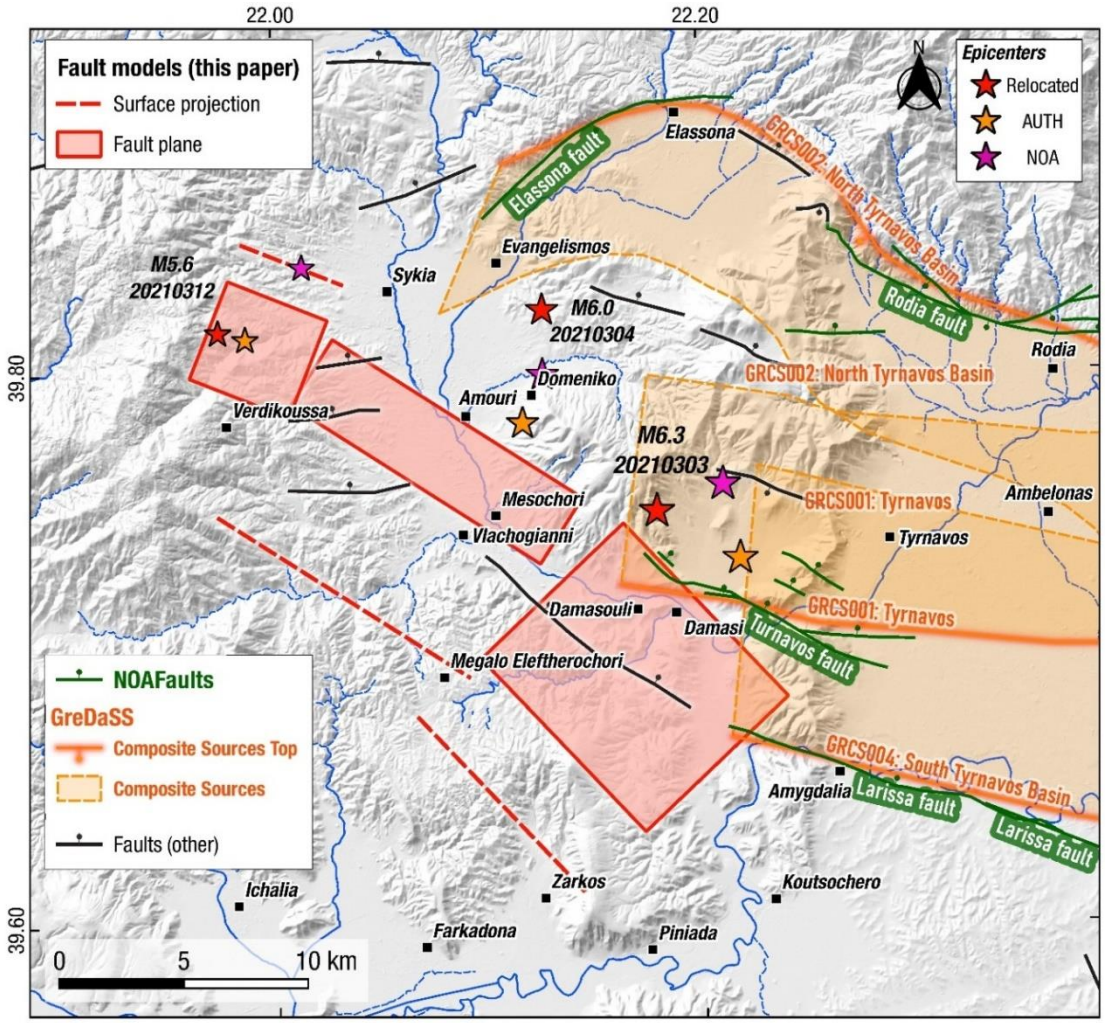

Fig. 15: Shaded relief map showing active faults according to the GreDASS (orange lines and shaded areas; Caputo and Pavlides, 2013) and NOAFAULTs databases (with ticks on the downthrown side). Solid stars indicate epicentres of the three main shocks. Rectangles indicate the surface projection of seismic faults (this study). *A high-resolution version of this figure is provided in the supplement section of this article*.

7.3 Ground cracks marking localized co-seismic and post-seismic deformation

On March 13, 2021 we mapped ground cracks at two locations north of village Zarko (Fig. 10 locality 4; Fig. 12d); about 4 km north of the village inside the Pelagonian basement rocks (schists and gneisses). At the second location (Fig. 12d; approx. 39.6460°N - 22.1251°E) we found two fracture traces, roughly oriented N-S. The fracture length is 15 m (Fig. 16). Then, each fracture trace was mapped in detail by means of a DEM created by close-range photogrammetric data (Fig. 16a). We used a camera Lenovo Tab M8 FHD and the Agisoft Photoscan 1.6.4 to process the data. The terrain model (cell-size 2 mm) was imported in ArcGIS Pro where the fracture trace was analysed for its spatial characteristics (orientation). In order to accurately measure the fracture's strike, we created 12 segments with a relatively homogeneous strike (Fig. 16b). Each fracture segment had its strike computed by the software using the entirety of its length.

We measured at 20 points the direction of fracture opening (the tension axis) using photogrammetry and we compared the findings with our field measurements (7 points; by use of a compass) at nearly identical sites. The measurements were imported in WinTensor v5.9.2 (Delvaux and Sperner, 2003) and rose diagrams were created showing the tensile axes azimuths (Fig. 16a) of both field and photogrammetry measurements. The azimuth of the mean tensile axis (Fig. 16a) is N75°E. In addition, detailed measurements of the fracture's azimuth were also taken, both photogrammetrically (12) and on site (7; Fig. 16b). The mean strike of the fracture is N343°E (a secondary strike is N320°E; Fig. 16b). The mean aperture (opening) of the cracks is 0.018 m (20 measurements).

Moreover, the Zarko ground cracks were mapped where we have observed a vanishing gradient on both the co-seismic and post-seismic interferograms of the 1st event (March 3, 2021 10:16 UTC; Fig. 6 and Fig. 17). This evidence suggests that the cracks are due to primary tectonic motion along the fault and they are not due to ground shaking. We attribute their formation to dilatational strains that develop at the tip of the rupture plane which we infer that it is located very close to the ground surface, perhaps a few hundred metres deep (see dashed red-line in Fig. 15). Other than this locality, we observed a lack of significant post-seismic deformation on our geodetic data. This is something different than the recent Aegean and Ionian Sea earthquakes (see a compilation in Briole et al. 2021; also, Ganas et al. 2021b). This lack of detectability of post-seismic deformation may be due to a combination of factors such as a) lack of GNSS stations near to the seismic faults (for example, in the Samos earthquake case the nearest GNSS station was located 4 km from the top-fault edge; Ganas et al. 2021b), b) the moderate magnitudes of the events ($5.6 \leq M \leq 6.3$) and c) the intermediate-angle of fault dip (ranging from 36° to 40°).

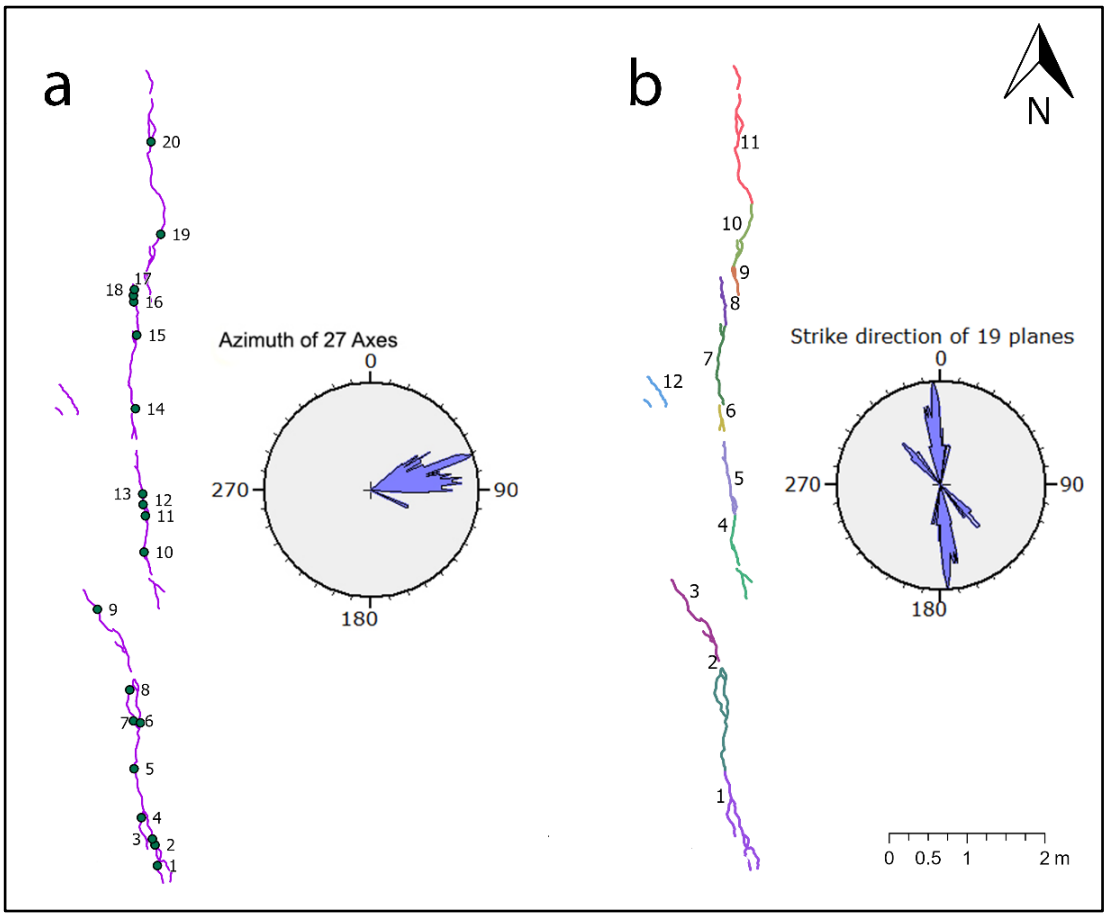

Fig. 16: Surface break data north of village Zarko a) the fracture trace consisting of two segments (thin purple lines) with points (green dots) where the tension axis was measured. The rose diagram (10° interval) shows the azimuths of the individual tensile axes (27 measurements in total) b) the fracture trace showing the 12 segment groups that were used for the calculation of the strike (19 measurements in total). See Fig. 12d for a field photograph. See Fig. 17 for location.

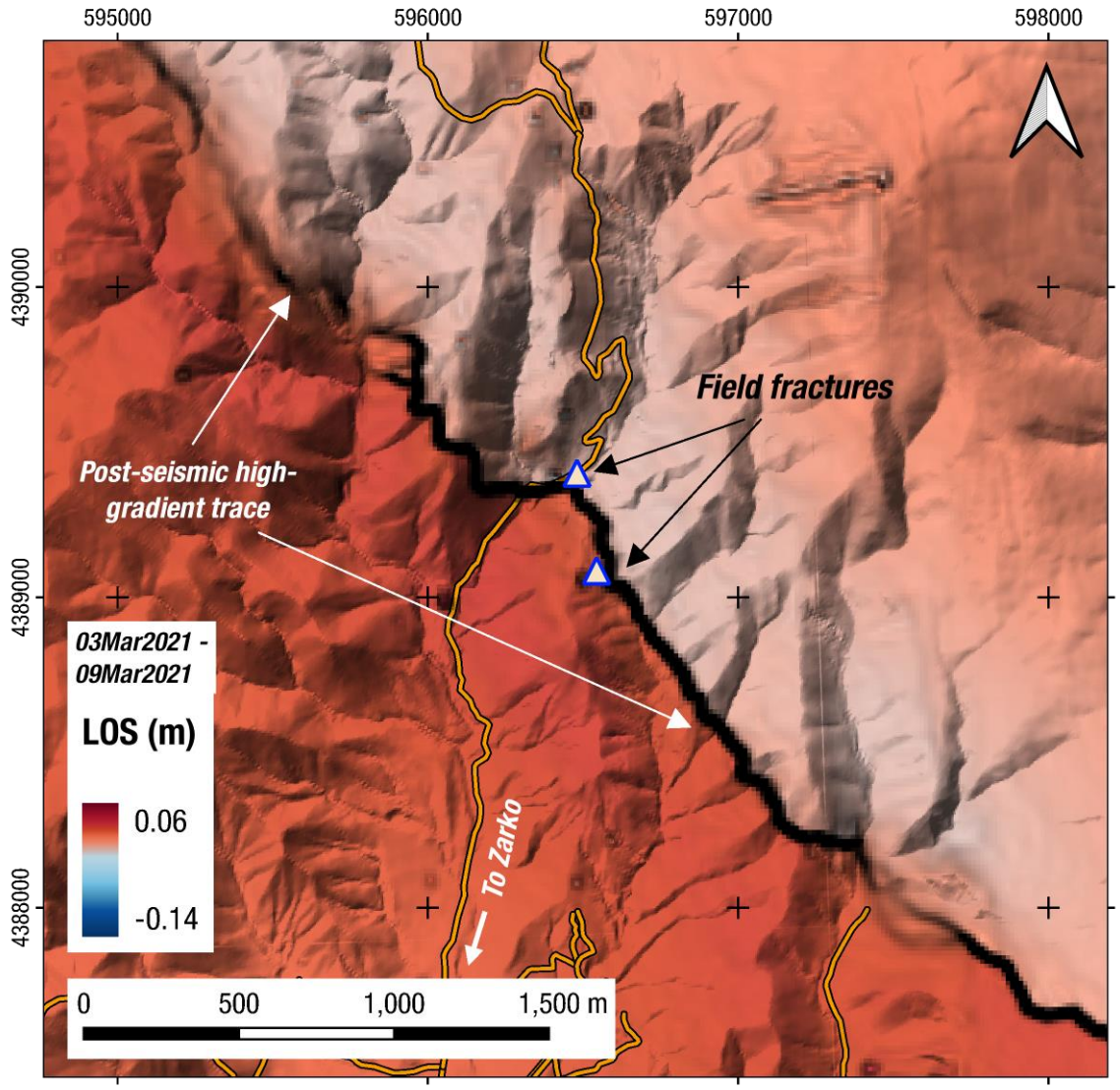

Fig. 17: Post-seismic interferogram (track 102, ascending orbit) showing alignment of phase gradient (thick black line) with location of surface cracks observed in the field (see Fig. 12d for a field photograph).

8. CONCLUSIONS

1. Our results indicate that the March 3, 2021 M_w=6.3 rupture occurred on a northeast-dipping, intermediate-angle normal fault located between the villages Zarko (Trikala) and Damasi (Larissa).
2. The event of March 4, 2021 M_w=6.0 occurred northwest of Damasi, along a fault oriented WNW-ESE and produced less deformation than the event of the previous day.
3. The third event (M_w=5.6) occurred on March 12, 2021 along a south-dipping normal fault.
4. The use of InSAR was crucial to differentiate the ground deformation between the ruptures. The majority of deformation occurs in the vertical component, with a maximum

of 0.39 m of subsidence over the M_w=6.3 rupture plane, south of Damasi. A total amount of 0.3 m horizontal displacement (E-W) was measured in the same region.

5. The inversion modelling of InSAR data indicates the activation of intermediate-angle normal faults, previously unknown.
6. No tectonic ruptures with lateral displacement were found in the field, in agreement with the modelled faults as blind structures.
7. We mapped two fracture sets to the north of village Zarko which comprise tensile cracks. We attribute their formation to dilatational strains that develop at the tip of the rupture plane which we infer that it is located very close to the ground surface,
8. Only the March 3, 2021 M_w=6.3 event produced significant displacement at the GNSS stations.
9. We made several post-seismic interferograms, but we have seen that there is almost no post-seismic deformation, except in the footwall area (Zarkos mountain; Fig. 17). In general, it is below the 7 mm level (quarter of fringe) in the near field and below the 1 mm level at the GNSS sites.
10. The March 2021 earthquakes generated numerous secondary phenomena with vast areas of alluvial deposits (mainly along the Piniada valley) exhibiting spectacular liquefaction features.

9. ACKNOWLEDGEMENTS

We are indebted to ESA and Copernicus for providing access to SAR images. We acknowledge the constructive reviews of Vassilis Karakostas, Ritsa Papadimitriou and Riccardo Caputo. We thank Efthimios Lekkas, Costas Papazachos, Ritsa Papadimitriou, Vasillis Karakostas, Spiros Pavlides, Ioannis Koukouvelas, Alekos Belesis and Dimitris Galanakis for comments and discussions in the field. GNSS data were provided by INGV, NOANET, HxGN Smartnet, AUTH-Hermes and Tree-Uranus networks. We are indebted to the local authorities of Tyrnavos, Elassona, Piniada and Zarko for their help. We used seismological data from the following seismic networks, HL (Institute of Geodynamics, National Observatory of Athens, doi: 10.7914/SN/HL), HP (University of Patras, doi: 10.7914/SN/HP), HT (Aristotle University of Thessaloniki, doi: 10.7914/SN/HT), HA (National and Kapodistrian University of Athens, doi: 10.7914/SN/HA), and HI Institute of Engineering Seismology and Earthquake Engineering, doi: 10.7914/SN/HI) networks. We thank the staff of the National Observatory of Athens, Institute of Geodynamics, for phase picking. Several figures were created by use of GMT (Wessel et al. 2019) and the QGIS Geographic Information System http://www.qgis.org .

10. REFERENCES

Argyrakis, P., Ganas, A., Valkaniotis, S., Tsioumas, V., Sagias, N., Psiloglou, B., 2020. Anthropogenically induced subsidence in Thessaly, central Greece: new evidence from GNSS data. *Nat. Hazards*, 102, 179–200. https://doi.org/10.1007/s11069-020-03917-w

Bertiger, W., Desai, S.D., Haines, B., Harvey, N., Moore, A.W., Owen, S., Weiss, J.P., 2010. Single receiver phase ambiguity resolution with GPS data. *J Geod*, 84, 327–337 https://doi.org/10.1007/s00190-010-0371-9

Briole, P., De Natale, G., Gaulon, R., Pingue, F., Scarpa, R., 1986. Inversion of geodetic data and seismicity associated with the Friuli earthquake sequence (1976-1977), *Annales Geophysicae*, 4(B4), 481-492.

Briole, P., 2017. Modelling of earthquake slip by inversion of GNSS and InSAR data assuming homogeneous elastic medium, *Zenodo*. http://doi.org/10.5281/zenodo.1098399

Briole, P., Ganas, A., Elias, P., Dimitrov, D., 2021. The GPS velocity field of the Aegean. New observations, contribution of the earthquakes, crustal blocks model. *Geophys. J. Int.* 226, 468–492. https://doi.org/10.1093/gji/ggab089

Caputo, R. 1990. Geological and structural study of the recent and active brittle deformation of the Neogene-Quaternary basins of Thessaly (Central Greece). *Scientific Annals, 2*, Aristotle University of Thessaloniki, Thessaloniki (1990), p. 255, 5 encl.

Caputo, R. 1993. Morphotectonics and kinematics along the Tirnavos fault, northern Larissa plain, mainland Greece, *Zeits. für Geomorph*. N.F., Suppl.-Bd., 94, pp. 167-185

Caputo, R., 1995. Inference of a seismic gap from geological data: Thessaly (Central Greece) as a case study. *Ann. Geofisc*., 38 (1), pp. 1-19, 10.4401/ag-4127

Caputo, R., 1996. The active Nea Anchialos Fault System (Central Greece): comparison of geological, morphotectonic, archaeological and seismological data. *Annali di Geofisica*, 39, 3, 557-574.

Caputo, R., and Pavlides, S., 1993. Late Cenozoic geodynamic evolution of Thessaly and surroundings (Central-Northern Greece). *Tectonophysics*, 223, 3-4, 339-362.

Caputo, R., B. Helly, S. Pavlides, G. Papadopoulos, 2004. Palaeoseismological investigation of the Tyrnavos Fault (Thessaly, Central Greece). *Tectonophysics*, 394 (1), pp. 1-20, 10.1016/j.tecto.2004.07.047.

Caputo, R., and Helly, B. 2005. Archaeological evidences of past earthquakes: a contribution to the SHA of Thessaly, Central Greece. *J. Earthq. Eng*., 9 (2), 199-222, 10.1080/13632460509350539

Caputo, R., Pavlides, S. 2013. The Greek Database of Seismogenic Sources (GreDaSS), version 2.0.0: A compilation of potential seismogenic sources (Mw>5.5) in the Aegean Region, 10.15160/unife/gredass/0200

Caputo, R., B. Helly, D. Rapti, S. Valkaniotis, 2021. Late Quaternary hydrographic evolution in Thessaly (Central Greece): The crucial role of the Piniada Valley. *Quaternary International*, https://doi.org/10.1016/j.quaint.2021.02.013.

Crotwell, H.P., Owens, T.J., Ritsema, J., 1999. The TauP Toolkit: Flexible Seismic Travel-time and Ray-path Utilities. *Seismol. Res. Lett*. 70, 154–160. https://doi.org/10.1785/gssrl.70.2.154

Dalla Via, G., Crosetto, M., Crippa, B. 2012. Resolving vertical and east-west horizontal motion from differential interferometric synthetic aperture radar: The L'Aquila earthquake. *J. Geophys. Res*., 117, B02310. https://doi.org/10.1029/2011JB008689

D'Agostino, N., M. Métois, R. Koci, L. Duni, N. Kuka, A. Ganas, I. Georgiev, F. Jouanne, N. Kaludjerovic, R. Kandić, 2020. Active crustal deformation and rotations in the southwestern Balkans from continuous GPS measurements. *Earth and Planetary Science Letters*, 539, 116246, https://doi.org/10.1016/j.epsl.2020.116246

Delvaux, D. and Sperner, B. 2003. Stress tensor inversion from fault kinematic indicators and focal mechanism data: the TENSOR program. In: New Insights into Structural Interpretation and Modelling (D. Nieuwland Ed.). Geological Society, London, Special Publications, 212, 75-100.

Drakatos, G., Papanastassiou, D., Voulgaris, N., Stavrakakis, G., 1998. Observations on the 3-D crustal velocity structure in the Kozani-Grevena (NW Greece) area. *J. Geodyn*. 26, 341–351. https://doi.org/10.1016/S0264-3707(97)00061-6

Ganas, A., Salvi, S., Atzori, S., Tolomei, C., 2006a. Ground deformation in Thessaly, Central Greece, retrieved from Differential Interferometric analysis of ERS-SAR data. *11th International Symposium on Natural and Human Induced Hazards & 2nd Workshop on Earthquake Prediction Abstract Volume, June 22-25, 2006, Patras, Greece*, page 41.

Ganas, A, Sokos, E, Agalos, A, Leontakianakos, G, Pavlides S, 2006b. Coulomb stress triggering of earthquakes along the Atalanti Fault, central Greece: Two April 1894 M6+ events and stress change patterns. *Tectonophysics*, 420, 357–369.

Ganas, A., G. Drakatos, S. Rontogianni, C. Tsimi, P. Petrou, M. Papanikolaou, P. Argyrakis, K. Boukouras, N. Melis and G. Stavrakakis, 2008. NOANET: the new permanent GPS network for Geodynamics in Greece. *Geophysical Research Abstracts*, Vol. 10, EGU2008-A-04380.

Ganas, A., 2020. NOAFAULTS KMZ layer Version 3.0 (2020 update) (Version V3.0) [Data set]. *Zenodo*. http://doi.org/10.5281/zenodo.4304613

Ganas, A., Valkaniotis S., Tsironi V., Karasante I., Elias P., Kapetanidis V., Kassaras I., Papathanassiou G. and Briole, P. 2021a. The March 2021 seismic sequence in Larisa - Damasi, Thessaly (central Greece), its seismotectonic characteristics and geodynamic effects. *Zenodo*. http://doi.org/10.5281/zenodo.4617264

Ganas, A., Elias, P., Briole, P., Valkaniotis, S., Escartin, J., Tsironi, V., Karasante, I., Kosma, C., 2021b. Co-seismic and post-seismic deformation, field observations and fault model of the 30 October 2020 Mw = 7.0 Samos earthquake, Aegean Sea. *Acta Geophys.* https://doi.org/10.1007/s11600-021-00599-1

Goldstein, R. M.; Werner, C. L. 1998. Radar interferogram filtering for geophysical applications. *Geophys. Res. Lett.* 25(21), 4035-4038.

Grigoriadis, V.N., Tziavos, I.N., Tsokas, G.N., Stampolidis, A., 2016. Gravity data inversion for Moho depth modeling in the Hellenic area. *Pure Appl. Geophys.* 173, 1223–1241. https://doi.org/10.1007/s00024-015-1174-y

Hatzfeld, D., Karakostas, Vassilios, Ziazia, M., Selvaggi, G., Leborgne, S., Berge, C., Guiguet, R., Paul, Anne, Voidomatis, P., Diagourtas, Dimitris, Kassaras, Ioannis, Koutsikos, I., Makropoulos, Kostas, Azzara, Riccardo, Bona, M., Baccheschi, S., Bernard, Pascal, Papaioannou, Christos, 1997. The Kozani- Grevena (Greece) Earthquake of 13 May 1995.

Revisited from a Detailed Seismological Study. *Bulletin of the Seismological Society of America*, 87, 473-473.

Hatzfeld, D., Ziazia, M., Kementzetzidou, D., Hatzidimitriou, P., Panagiotopoulos, D., Makropoulos, K., 1999. Microseismicity and focal mechanisms at the western termination of the North Anatolian Fault and their implications for continental tectonics, *Geophysical Journal International*, Volume 137, Issue 3, pp. 891-908.

Jackson, J. A., Gagnepain, J., Houseman, G., King, G. C. P., Papadimitriou, P., Soufleris, C., & Virieux, J. 1982. Seismicity, normal faulting, and the geomorphological development of the Gulf of Corinth (Greece) the Corinth earthquakes of February and March 1981. *Earth and Planetary Science Letters*, 57(2), 377– 397. https://doi.org/10.1016/0012-821X(82)90158-3

Kapetanidis, V., 2017. Spatiotemporal patterns of microseismicity for the identification of active fault structures using seismic waveform cross-correlation and double-difference relocation, PhD Thesis, National and Kapodistrian University of Athens.

Kapetanidis, V., Kassaras, I., 2019. Contemporary crustal stress of the Greek region deduced from earthquake focal mechanisms. *J. Geodyn.* 123, 55–82. https://doi.org/10.1016/j.jog.2018.11.004

Karakostas, C., Klimis, N., Lekidis, V., Makra, K., Margaris, B., Morfidis, K., Papaioannou, C., Rovithis, E., Salonikios, T., Sotiriadis, D., Theodoulidis, N., 2021. ΟΙ ΣΕΙΣΜΟΙ ΤΗΣ ΘΕΣΣΑΛΙΑΣ - Μ6.3, 3 Μαρτίου 2021 και Μ6.1, 4 Μαρτίου 2021. Προκαταρκτική έκθεση. https://doi.org/10.5281/ZENODO.4641200

Karastathis, V., Papoulia, J., Di Fiore, B., Makris, J., Tsampas, A., Stampolidis, A., Papadopoulos, G., 2011. Deep structure investigations of the geothermal field of the North Euboean Gulf, Greece, using 3-D local earthquake tomography and Curie Point Depth analysis. *Journal of Volcanology and Geothermal Research*, 206. https://doi.org/10.1016/j.jvolgeores.2011.06.008

Kilias A., Mountrakis D., 1989. The Pelagonian nappe. Tectonics, metamorphism and magmatism. (In Greek with English abstract). Bull. Geol. Soc. Greece, 23(1), 29-46.

King, G. C. P., Stein, R. S., and Rundle, J. B. 1988. The Growth of Geological Structures by Repeated Earthquakes 1. Conceptual Framework, *J. Geophys. Res.*, 93 (B11), 13307– 13318, doi:10.1029/JB093iB11p13307.

King, G.C.P., Stein, R.S., Lin, J., 1994. Static stress changes and the triggering of earthquakes, *Bull. Seism. Soc. Am.*, 84(3), 935-953.

Kiratzi, A.A., Wagner, G.S., Langston, C.A. 1991. Source parameters of some large earthquakes in Northern Aegean determined by body waveform inversion. Pure Appl. Geophys. *PAGEOPH* 135, 515–527, https://doi.org/10.1007/BF01772403

Konstantinou, K.I, 2017. Accurate relocation of seismicity along the North Aegean Trough and its relation to active tectonics. *Tectonophysics*, 717, 372-382.

Konstantinou, K. I., V. Mouslopoulou, W.-T. Liang, O. Heidbach, O. Oncken, and J. Suppe 2016. Present-day crustal stress field in Greece inferred from regional-scale damped inversion of earthquake focal mechanisms. *J. Geophys. Res. Solid Earth*, 121, doi:10.1002/2016JB013272.

Lekkas, E.L., Mavroulis, S.D. 2016. Fault zones ruptured during the early 2014 Cephalonia Island (Ionian Sea, Western Greece) earthquakes (January 26 and February 3, Mw 6.0) based on the associated co-seismic surface ruptures. *J Seismol* 20, 63–78. https://doi.org/10.1007/s10950-015-9510-3

Lekkas, E., K. Agorastos, S. Mavroulis, Ch. Kranis, Emm. Skourtsos, P. Carydis, M. Gogou, K.-N. Katsetsiadou, G. Papadopoulos, I. Triantafyllou, A. Agalos, S. Moraitis, E. Stamati, D. Psarris, G. Kaviris, V. Kapetanidis, P. Papadimitriou, A. Karakonstantis, I. Spingos, V. Kouskouna, I. Kassaras, K. Pavlou, N. Voulgaris, M. Mavrouli, S. Pavlides, A. Chatzipetros, S. Sboras, E. Kremastas, A. Chatziioannou, A. Kiratzi, C. Papazachos, N. Chatzis, V. Karakostas, E. Papadimitriou, I. Koukouvelas, K. Nikolakopoulos, A. Kyriou, D. Apostolopoulos, V. Zygouri, S. Verroios, A. Belesis, I. Tsentzos, P. Krassakis, K. Lymperopoulos, A. Karavias, D. Bafi, T. Gatsios, M. Karatzia, I. Gkougkoustamos, T. Falaras, I. Parcharidis, G. Papathanassiou, C.P. Evangelidis, V. Karastathis, G-A. Tselentis, A. Ganas, V. Tsironi, I. Karasante, S. Valkaniotis, D. Galanakis, G. Kostantopoulou, N. Theodoulidis, Ch. Karakostas, V. Lekidis, K. Makra, V. Margaris, K. Morfidis, Ch. Papaioannou, M. Rovithis, Th. Salonikios, N. Papadopoulos, A. Kourou, M. Manousaki, T. Thoma 2021. The early March 2021 Thessaly earthquake sequence. *Newsletter of Environmental, Disaster and Crises Management Strategies*, 22, ISSN 2653-9454.

Lomax, A., 2014. Seisgram2K, Seismogram visualization and analysis software version 7.0, http://alomax.free.fr/seisgram/SeisGram2K.html

Mantovani, A., Valkaniotis, S., Rapti, D. et al. 2018. Mapping the Palaeo-Piniada Valley, Central Greece, Based on Systematic Microtremor Analyses. *Pure Appl. Geophys*. 175, 865–881. https://doi.org/10.1007/s00024-017-1731-7

Migiros, G. 1985. Geological map of Greece in 1:50,000 scale, map sheet Gonnoi. Institute of Geological & Mineralogical Exploration, Athens.

Mountrakis, D., 1984. Structural evolution of the Pelagonian Zone in Northwestern Macedonia, Greece. *Geological Society, London, Special Publications*, 17, 581-590, https://doi.org/10.1144/GSL.SP.1984.017.01.45

Mountrakis, D., Kilias, A., Pavlides, S., Zouros, N., Spyropoulos, N, Tranos, M., and Soulakelis, N. 1993. Field study of the southern Thessaly highly active fault zone, in Proc. *2nd Congress Hellenic Geophys. Union*, 2, 603-614.

Müller, M.D., A. Geiger, H.G. Kahle, G. Veis, H. Billiris, D. Paradissis, S. Felekis, 2013. Velocity and deformation fields in the North Aegean domain, Greece, and implications for fault kinematics, derived from GPS data 1993–2009. *Tectonophysics*, 597, pp. 34-49.

Novotný, O., Zahradník, J., Tselentis, G.-A. 2001. Northwestern Turkey Earthquakes and the Crustal Structure Inferred from Surface Waves Observed in Western Greece. *Bulletin of the Seismological Society of America*, 91(4), 875–879. https://doi.org/10.1785/0120000116

Okada Y., 1992. Internal deformation due to shear and tensile faults in a half space, *Bull. Seism. Soc. America*, 82, 1018–1040.

Palyvos, N., Pavlopoulos, K., Froussou, E., Kranis, H., Pustovoytov, K., Forman, S.L., Minos-Minopoulos, D., 2010. Paleoseismological investigation of the oblique-normal Ekkara ground rupture zone accompanying the M 6.7–7.0 earthquake on 30 April 1954 in Thessaly, Greece: Archaeological and geochronological constraints on ground rupture recurrence. *J. Geophys. Res*. 115, B06301. https://doi.org/10.1029/2009JB006374

Papadimitriou, E.E, Karakostas, VG., 2003. Episodic occurrence of strong (Mw≥6.2) earthquakes in Thessalia area (central Greece), *Earth and Planetary Science Letters*, Volume 215, Issues 3–4, 395-409, https://doi.org/10.1016/S0012-821X(03)00456-4.

Papastamatiou, D., Mouyaris, N., 1986. The earthquake of April 30, 1954, in Sophades (Central Greece). *Geophys. J. R. astr. Soc.*, 87, 885-895.

Papazachos, B.C., Panagiotopoulos, D.G., Tsapanos, T.M., Mountrakis, D.M., Dimopoulos, G.C., 1983. A study of the 1980 summer seismic sequence in the Magnesia region of Central Greece. *Geophys. Jour. R. astron. Soc. London*, 75, 155-168.

Papazachos, B.C., P.M. Hatzidimitriou, G.F. Karakaisis, C.B. Papazachos, G.N. Tsokas, 1993. Rupture zones and active crustal deformation in southern Thessalia, central Greece, *Boll. Geof. Teor. Appl*. 139, 363-374.

Pavlides S., 1993. Active faulting in multi-fractured seismogenic areas; examples from Greece. *Z. Geomorph*. N. E., 94, 57-72.

Pavlides, S., Kouskouna, V., Ganas, A., Caputo, R., Karastathis, V., Sokos, E., 2004. The Gonnoi (NE Thessaly - Greece) Earthquake (June 2003, Ms=5.5) and the Neotectonic Regime of Lower Olympus. *5th International Symposium on Eastern Mediterranean Geology, Thessaloniki, Greece, 14-20 April 2004*, 627-630.

Plastiras, V. 1985. Geological map of Greece in 1:50,000 scale, map sheet Larissa. Institute of Geological & Mineralogical Exploration, Athens.

Rigo, A., Chabalier, J.-B. de, Meyer, B., Armijo, R., 2004. The 1995 Kozani-Grevena (northern Greece) earthquake revisited: an improved faulting model from synthetic aperture radar interferometry. *Geophys. J. Int*. 157, 727–736. https://doi.org/10.1111/j.1365-246X.2004.02220.x

Salvi, S., Ganas, A., Stramondo, S., Atzori, S., Tolomei, C., Pepe, A., Manzo, M., Casu, F., Berardino, P., Lanari, R., 2004. Monitoring Long-Term Ground Deformation by SAR Interferometry: Examples from the Abruzzi, Central Italy, and Thessaly, Greece. *5th International Symposium on Eastern Mediterranean Geology, Thessaloniki, Greece, 14-20 April 2004*, Reference T7-17.

Soufleris, C., J.A Jackson, G.C.P King, C Spencer, C Scholz, 1982. The 1978 earthquake sequence near Thessaloniki (northern Greece). *Geophysical Journal of the Royal Astronomical Society*, 68 (1982), pp. 429-458.

Stamatis, A. 1987. Geological map of Greece in 1:50,000 scale, map sheet Deskati. Institute of Geological & Mineralogical Exploration, Athens.

Taymaz, T., Jackson, J.A., McKenzie, D., 1991. Active tectonics of the north and central Aegean Sea, *Geophys. J. Int*., 106, 433-490.

Taymaz, T., Ganas, A., Yolsal-Çevikbilen, S., Vera, F., Eken, T., Erman, C., Keleş, D., Kapetanidis, V., Valkaniotis, S., Karasante, I., Tsironi, V., Gaebler, P., Melgar, D., Ocalan, T., 2021. Source Mechanism and Rupture Process of the 24 January 2020 Mw 6.7 Doğanyol-Sivrice Earthquake obtained from Seismological Waveform Analysis and Space Geodetic Observations on the East Anatolian Fault Zone (Turkey), *Tectonophysics*, https://doi.org/10.1016/j.tecto.2021.228745

Toda, S., Stein, R.S., Sevilgen, V., Lin, J., 2011. Coulomb 3.3 Graphic-rich deformation and stress-change software for earthquake, tectonic, and volcano research and teaching-user guide. U.S. Geological Survey Open-File Report 2011-1060, 63, http://pubs.usgs.gov/of/2011/1060/

Tolomei C., Caputo R., Polcari M., Famiglietti NA., Maggini M., Stramondo S., 2021. The Use of Interferometric Synthetic Aperture Radar for Isolating the Contribution of Major Shocks: The Case of the March 2021 Thessaly, Greece, Seismic Sequence. *Geosciences*. 11(5):191. https://doi.org/10.3390/geosciences11050191

Tranos, M., E. Papadimitriou, A. Kilias, 2003. Thessaloniki-Gerakarou Fault Zone (TGFZ): the western extension of the 1978 Thessaloniki earthquake fault (northern Greece) and seismic hazard assessment. *J. Struct. Geol*., 25, pp. 2109-2123

Triantafillis, E. 1987. Geological map of Greece in 1:50,000 scale, map sheet Elassona. Institute of Geological & Mineralogical Exploration, Athens.

Tsodoulos, I.M., K. Stamoulis, R. Caputo, I. Koukouvelas, A. Chatzipetros, S. Pavlides, C. Gallousi, C. Papachristodoulou, K. Ioannides, 2016. Middle-Late Holocene earthquake history of the Gyrtoni Fault, Central Greece: insight from optically stimulated luminescence (OSL) dating and paleoseismology, *Tectonophysics*, 687, 14-27, 10.1016/j.tecto.2016.08.015

Valkaniotis S., Ganas A., Papathanassiou, G., and Papanikolaou M., 2014. Field observations of geological effects triggered by the January-February 2014 Cephalonia (Ionian Sea, Greece) earthquakes, *Tectonophysics*, 630, 150-157, DOI:10.1016/j.tecto.2014.05.012

Valkaniotis, S., Papathanassiou, G., Ganas, A., Kremastas, E., Caputo, R., 2021. Preliminary report of liquefaction phenomena triggered by the March 2021 earthquakes in Central Thessaly, Greece. https://doi.org/10.5281/ZENODO.4608365 released (2021, March 16).

Veci, L., Lu, J., Prats-Iraola, P., Scheiber, R., Collard, F., Fomferra, N., Engdahl, M., 2014. The Sentinel-1 toolbox. In: *Proceedings of the IEEE International Geoscience and Remote Sensing Symposium (IGARSS). IEEE*, pp. 1–3.

Vidakis, M. 1998. Geological map of Greece in 1:50,000 scale, map sheet Farkadona. Institute of Geological & Mineralogical Exploration, Athens.

Waldhauser, F., 2001. hypoDD—A Program to Compute Double-Difference Hypocenter Locations: U.S. Geological Survey Open-File Report 01-113, 25 pp., https://pubs.usgs.gov/of/2001/0113/ .

Waldhauser, F., Ellsworth, W. L. 2000. A Double-difference Earthquake location algorithm: Method and application to the Northern Hayward Fault, California. *Bulletin of the Seismological Society of America*, 90(6), 1353–1368. https://doi.org/10.1785/0120000006

Wessel, P., Luis, J. F., Uieda, L., Scharroo, R., Wobbe, F., Smith, W. H. F., Tian, D. 2019. The Generic Mapping Tools version 6. *Geochemistry, Geophysics, Geosystems*, 20, 5556–5564.

Wright, T.J., Parsons, B., Lu, Z. 2004. Toward mapping surface deformation in three dimensions using InSAR. *Geophysical Research Letters*, 31 (1), L01607. https://doi.org/10.1029/2003GL018827

Table S1. List with relocation data for the three main events of the March 2021 northern Thessaly sequence. Time is UTC.

Event	LAT (°)	LON (°)	DEPTH (km)	YEAR	MO	DAY	Hr	Min	SS.SS	M_L (NOA)
1	39.7495	22.1791	10.7	2021	3	3	10	16	7.400	6.0
2	39.8227	22.1261	13.0	2021	3	4	18	38	16.600	5.9
3	39.8152	21.9738	7.1	2021	3	12	12	57	49.060	5.2

Table S2. Focal mechanisms of 22 aftershocks with M≥4.0.

Year	Mo	Day	Hr	Mn	Sec	Latitude	Longitude	Dep	Mag	Strike1	Dip1	Rake1	Strike2	Dip2	Rake2
2021	3	3	10	20	45.93	39.694	22.174	9.4	4.7	178.8	49.5	-43.8	300.7	58.2	-130.2
2021	3	3	10	23	8.12	39.692	22.154	10.4	4.1	267.5	47.0	-139.7	147.5	61.8	-50.7
2021	3	3	10	26	18.33	39.641	22.218	9.7	4.1	2.8	52.9	-37.8	117.9	60.7	-136.3
2021	3	3	10	34	7.54	39.707	22.232	11.7	4.9	283.0	56.1	-148.8	174.3	64.5	-38.2
2021	3	3	11	12	23.08	39.707	22.150	10.3	4.3	327.1	50.8	-41.6	86.4	59.0	-132.5
2021	3	3	11	35	56.66	39.691	22.208	10.2	4.8	344.4	44.7	-87.5	160.9	45.4	-92.5
2021	3	3	18	24	8.06	39.723	22.087	11.6	5.2	328.6	54.0	-34.7	80.7	62.6	-138.5
2021	3	3	18	49	48.25	39.734	22.101	12.4	4.2	77.7	33.7	-92.0	260.1	56.3	-88.7
2021	3	3	21	0	54.67	39.748	22.127	10.2	4.0	278.3	43.7	-145.3	161.7	66.8	-51.8
2021	3	4	2	43	37.77	39.719	22.221	11.6	4.0	349.1	36.7	-71.0	145.9	55.6	-103.6
2021	3	4	9	36	15.37	39.782	22.123	13.2	4.4	130.9	48.0	-35.9	246.7	64.2	-132.0
2021	3	4	18	45	26.58	39.828	22.000	11.9	4.1	242.0	51.4	-150.8	132.8	67.6	-42.4
2021	3	4	19	23	50.99	39.829	21.927	11.6	5.0	248.8	41.9	-101.6	84.2	49.1	-79.8
2021	3	4	19	31	31.96	39.801	22.039	11.5	4.2	125.0	52.7	-38.4	240.7	60.4	-135.8
2021	3	4	20	3	8.11	39.729	22.115	11.1	4.2	331.7	53.5	-29.4	80.2	66.8	-139.7
2021	3	5	9	59	58.96	39.825	22.021	15.1	4.2	86.0	41.7	-85.4	259.8	48.5	-94.1
2021	3	5	10	1	14.49	39.768	22.076	10.3	4.2	294.8	36.0	-84.3	107.8	54.2	-94.1
2021	3	6	16	36	17.51	39.659	22.243	11.6	4.1	356.0	65.3	-22.9	96.0	69.3	-153.5
2021	3	6	19	47	39.76	39.829	22.064	9.6	4.1	3.7	47.9	-34.6	118.5	65.1	-132.3
2021	3	11	14	19	40.40	39.768	22.076	6.3	4.0	124.4	46.9	-42.0	246.0	60.8	-128.5
2021	3	15	15	43	37.71	39.762	22.149	8.0	4.3	263.2	24.5	-86.2	79.0	65.6	-91.7
2021	3	21	17	15	54.04	39.771	22.102	8.8	4.1	287.5	42.3	-69.4	80.6	51.0	-107.8

Fig. S1: Magnitude distribution histogram of the relocated events (M_L after National Observatory of Athens manual measurements).

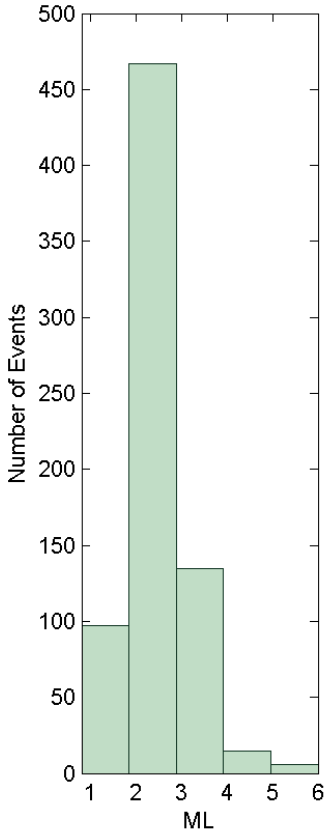

Fig. S2: Graph showing East, North, Up position time series of station KLOK during the period of the 2nd event (March 4, 2021 18:38 UTC).

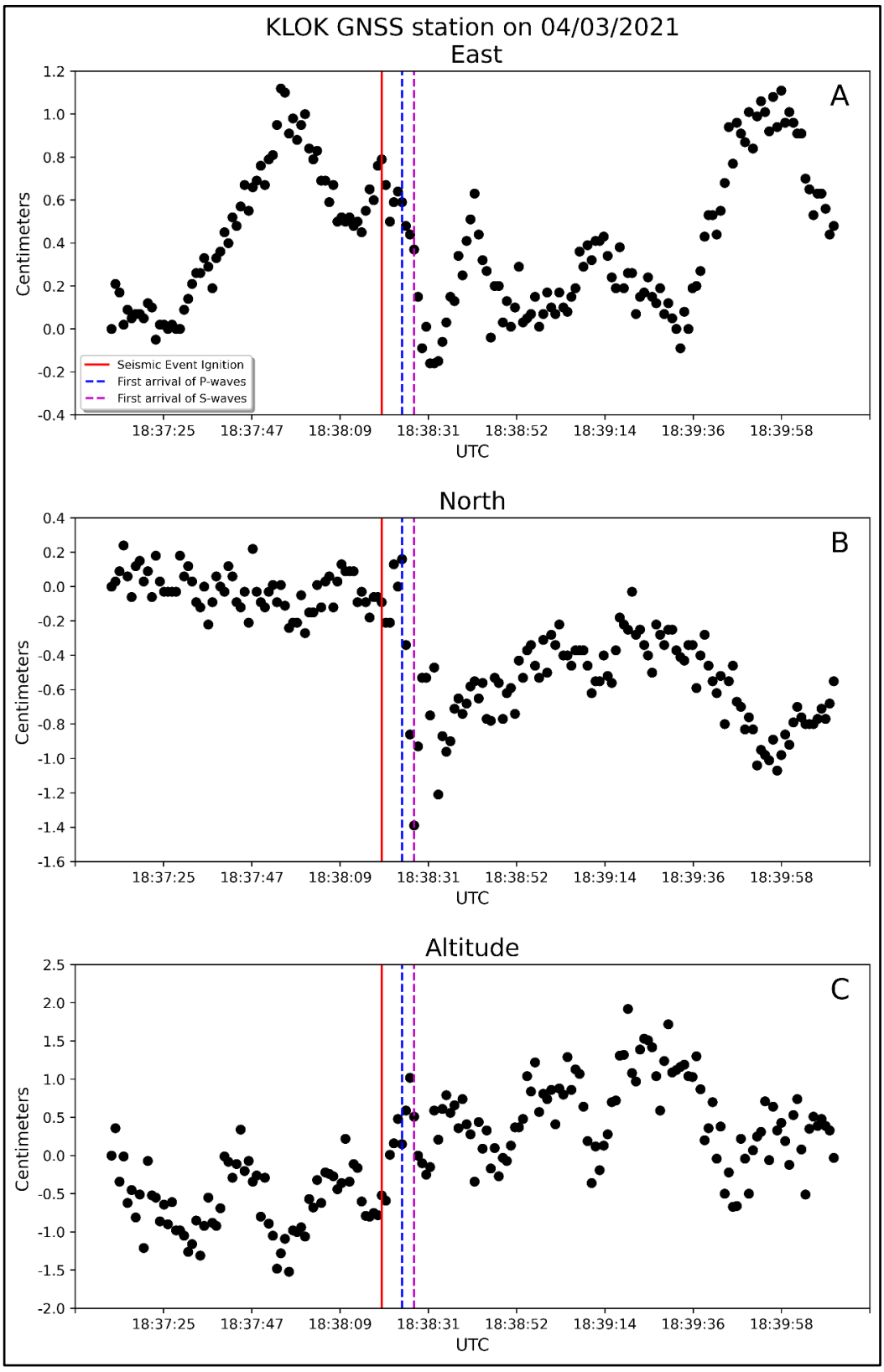

Fig. S3: Coulomb stress transfer on optimally-oriented planes to regional extension (N183.9°E). Calculation at a depth of 9 km.

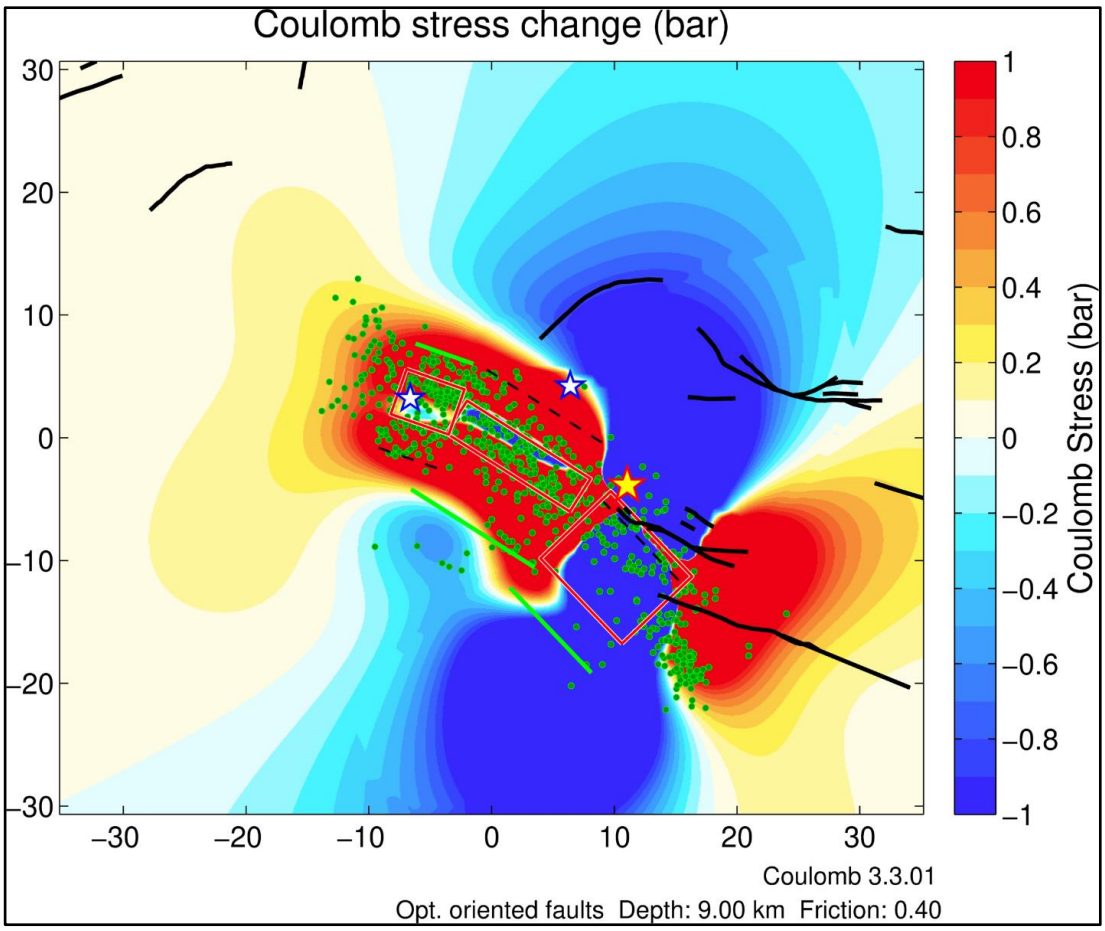

Fig. S4: Vertical cross-sections of Coulomb stress transfer through the fault planes of Fig. 14. The green line shows the respective fault plane. Stars denote the hypocentre of the respective major earthquake, while green circles represent smaller aftershocks. Horizontal dashed line shows the depth of 9 km where map slices are shown in Fig. 14.